

Disk Substructures at High Angular Resolution Project (DSHARP): **author order WILL change!**
I. Motivation, Sample, Calibration, and Overview (**just working on layout**)

SEAN M. ANDREWS,¹ XUE-NING BAI,^{2,3} M. BENISTY,^{4,5,6} T. BIRNSTIEL,⁷ JOHN M. CARPENTER,⁸ C. P. DULLEMOND,⁹ V. V. GUZMÁN,⁸ JANE HUANG,¹ A. MEREDITH HUGHES,¹⁰ ANDREA ISELLA,¹¹ KARIN I. ÖBERG,¹ LAURA M. PÉREZ,⁵ LUCA RICCI,¹² NICOLÁS TRONCOSO,⁵ ERIK WEAVER,¹¹ DAVID J. WILNER,¹ SHANGJIA ZHANG,¹³ AND ZHAOHUAN ZHU¹³

¹ *Harvard-Smithsonian Center for Astrophysics, 60 Garden Street, Cambridge, MA 02138, USA*

² *Institute for Advanced Study, Tsinghua University, Beijing 100084, China*

³ *Tsinghua Center for Astrophysics, Tsinghua University, Beijing 100084, China*

⁴ *Unidad Mixta Internacional Franco-Chilena de Astronomía, CNRS/INSU UMI 3386*

⁵ *Departamento de Astronomía, Universidad de Chile, Casilla 36-D, Santiago, Chile*

⁶ *Univ. Grenoble Alpes, CNRS, IPAG, 38000 Grenoble, France*

⁷ *University Observatory, Faculty of Physics, Ludwig-Maximilians-Universität München, Scheinerstr. 1, 81679 Munich, Germany*

⁸ *Joint ALMA Observatory, Avenida Alonso de Córdova 3107, Vitacura, Santiago, Chile*

⁹ *Heidelberg University, Center for Astronomy, Albert Ueberle Str 2, Heidelberg, Germany*

¹⁰ *Department of Astronomy, Van Vleck Observatory, Wesleyan University, 96 Foss Hill Drive, Middletown, CT 06459, USA*

¹¹ *Department of Physics and Astronomy, Rice University, 6100 Main Street, Houston, TX 77005, USA*

¹² *Jet Propulsion Laboratory, California Institute of Technology, 4800 Oak Grove Drive, Pasadena, CA 91106, USA*

¹³ *Department of Physics and Astronomy, University of Nevada, Las Vegas, 4505 S. Maryland Pkwy, Las Vegas, NV 89154, USA*

ABSTRACT

We introduce the Disk Substructures at High Angular Resolution Project (DSHARP), one of the initial Large Programs conducted with the Atacama Large Millimeter/submillimeter Array (ALMA). The primary goal of DSHARP is to find and characterize *substructures* in the spatial distributions of solid particles for a sample of 20 nearby protoplanetary disks, using very high resolution ($\sim 0''.035$, or 5 au, scales) observations of their 240 GHz (1.25 mm) continuum emission. These data provide a first homogenized look at the small-scale features in disks that are directly relevant to the planet formation process, quantifying their prevalence, morphologies, spatial scales, spacings, symmetry, and amplitudes, for targets with a variety of disk and stellar host properties. We find that these substructures are ubiquitous in this sample. They are most frequently manifested as concentric, narrow emission rings and depleted gaps, although large-scale spiral patterns and small arc-like azimuthal asymmetries are also present in some cases. These substructures are found at a wide range of disk radii, from a few au to more than 100 au, and are usually small ($\lesssim 10$ au) and have modest brightness contrasts (\lesssim tens of percent). Here we discuss the motivation for the project, describe the survey design and the sample properties, detail the observations and data calibration, highlight some basic observational results, and provide a general overview of the key conclusions presented in more detail in a series of accompanying articles. The DSHARP data – including calibrated visibilities, images, and associated scripts – have been released online for community use at <http://almascience.nrao.edu/alma-data/DSHARP>.

Keywords: protoplanetary disks — circumstellar matter — planets and satellites: formation — submillimeter: planetary systems

1. INTRODUCTION

There is a long-standing desire to link the properties of circumstellar disks with the initial conditions of planetary systems. The theoretical aspiration in the field is to develop a deterministic framework that takes a set of measured disk properties (e.g., Andrews et al. 2009, 2010; Isella et al. 2009, 2010) and predicts the characteristics of the exoplanet population (e.g., Ida & Lin 2004, 2008; Alibert et al. 2005; Mordasini et al. 2009). A quality reproduction in this population synthesis context

requires the tuning of increasingly sophisticated models for the formation of planetary systems, their interactions with disk material, and their subsequent long-term dynamical evolution (Benz et al. 2014).

From an efficiency standpoint, the most crucial challenge in standard planet formation models is the ability to make planetesimals (Johansen et al. 2014). The formation of terrestrial planets and giant planet cores hinges on the *rapid* agglomeration of small solid particles into larger (\gg km-sized) planetesimals. Astronomers have worked on this topic and its many pitfalls for more

than 50 years, although without much observational guidance. Fortunately, that is now changing. High resolution observations of the continuum emission from mm/cm-sized particles measure how these solids are spatially distributed in disks, exposing substantial radial gradients in their particle size distributions (larger particles closer to the host star; Isella et al. 2010; Guilloteau et al. 2011; Pérez et al. 2012, 2015; Menu et al. 2014; Tazzari et al. 2016; Tripathi et al. 2018) and solids-to-gas ratios (higher closer to the host star; Panić et al. 2009; Andrews et al. 2012; de Gregorio-Monsalvo et al. 2013; Rosenfeld et al. 2013; Zhang et al. 2014; Facchini et al. 2017; Ansdell et al. 2018). Those measurements provide strong empirical support for models of the growth and migration of solids early in the planetesimal assembly process (e.g., Birnstiel & Andrews 2014; Testi et al. 2014; Birnstiel et al. 2016).

Despite that progress, there is still considerable tension regarding the planetesimal formation timescales for the default assumption of a smooth gas disk (with pressure decreasing monotonically with radius, r). This tension is associated with *radial drift*, the inward migration of solids toward the global pressure maximum that occurs when they decouple from the sub-Keplerian gas flow (e.g., Adachi et al. 1976; Weidenschilling 1977; Nakagawa et al. 1986). The predicted drift rates for mm/cm-sized solids located tens of au from the host star are fast enough to severely limit planetesimal growth outside a few au (Takeuchi & Lin 2002, 2005; Brauer et al. 2007, 2008) and are in apparent conflict with observations that routinely find emission from those particles at $r \approx 10$ –100 au (e.g., Tripathi et al. 2017; Tazzari et al. 2017; Barenfeld et al. 2017; Andrews et al. 2018).

This dilemma and contradiction suggest that the assumption of a smooth gas disk is inappropriate. Localized modulations of the gas pressure can slow or trap drifting solids (Whipple 1972; Pinilla et al. 2012), perhaps concentrating them enough to drive an instability that rapidly converts pebbles to planetesimals (e.g., Youdin & Shu 2002; Youdin & Goodman 2005; Johansen et al. 2009). Such pressure modulations (or even other migration bottlenecks) could be produced by fluid instabilities (e.g., Dzyurkevich et al. 2013; Bai 2014; Dipierro et al. 2015; Dullemond & Penzlin 2018) or strong gradients in material properties (e.g., Okuzumi et al. 2012; Flock et al. 2015; Lyra et al. 2015; Armitage et al. 2016; Stammler et al. 2017; Pinilla et al. 2017). Their roles in regulating the migration of solids and facilitating the rapid growth of planetesimals indicate that these small-scale material concentrations – *substructures* – are fundamental aspects of planet formation. If substructures are produced early, it may be possible that the typical \sim Myr-old disk already contains a nascent planetary system that generates its own substructures from its interactions with disk material (e.g., Greaves & Rice 2010; Najita & Kenyon 2014; Nixon et al. 2018). Observations of disk substructures are essential for characterizing the

mechanisms that concentrate solids, and thereby for integrating a robust model of planetesimal formation into the broader theoretical framework for understanding the birth and evolution of planetary systems.

Direct observations of small-scale gas pressure variations in disks based on high resolution measurements of molecular line emission are a formidable challenge. However, the particle trapping capabilities of even modest pressure maxima should substantially amplify the associated local mm/cm-sized particle density (e.g., Paardekooper & Mellema 2006; Rice et al. 2006; Pinilla et al. 2012; Zhu et al. 2012), generating a bright signature in the broadband (sub-)mm continuum that is much easier to measure on the smallest scales. The initial foray into such work came from the sub-population of “transition” disks (Strom et al. 1989; Skrutskie et al. 1990; Calvet et al. 2002), which show dense particle rings at $r \approx$ tens of au outside, bordering dust-depleted central cavities (e.g., Andrews et al. 2011; van der Marel et al. 2018; Pinilla et al. 2018). Observations with sufficient sensitivity and resolution reveal that these ring-shaped particle traps also exhibit complex substructures, including azimuthal asymmetries (Casassus et al. 2013; van der Marel et al. 2013; Isella et al. 2013; Pérez et al. 2014), additional rings (Fedele et al. 2017; van der Plas et al. 2017), warped geometries (and/or radial inflows; Rosenfeld et al. 2012, 2014; Marino et al. 2015; Casassus et al. 2018), and spiral arm extensions (Christiaens et al. 2014; van der Marel et al. 2016). Similar features have also been identified from the infrared starlight scattered off the disk atmospheres (e.g., Muto et al. 2012; Grady et al. 2013; Quanz et al. 2013; Avenhaus et al. 2014; Benisty et al. 2015; de Boer et al. 2016; Ginski et al. 2016; Akiyama et al. 2016).

A series of serendipitous discoveries at modest (\sim 10–20 au) resolution make it apparent that the general disk population (i.e., *not* transition disks) also exhibit small-scale substructures in the forms of rings/gaps (Zhang et al. 2016; Isella et al. 2016; Cieza et al. 2016, 2017; Loomis et al. 2017; Huang et al. 2017; Cox et al. 2017; Dipierro et al. 2018; Fedele et al. 2018; van Terwisga et al. 2018) and spirals (Pérez et al. 2016). The richness of these substructures becomes clear for the few individual cases to date that have had their continuum emission probed at resolutions of only a few au (HL Tau, ALMA Partnership et al. 2015; TW Hya, Andrews et al. 2016; MWC 758, Dong et al. 2018). Again, similar conclusions are being drawn from infrared scattered light measurements (e.g., Avenhaus et al. 2018).

All of these observations suggest that substructures are common, and therefore are likely to play significant roles in the coupled disk evolution and planet formation processes. Moreover, they demonstrate a tremendous opportunity: high resolution (sub-)mm continuum measurements can be used to quantify the forms, prevalence, and diversity (e.g., in scales, locations, amplitudes) of disk substructures, and thereby to aid in the develop-

ment of a more robust theoretical framework for characterizing the early evolution of planetary systems. The next step along that path is to move from a serendipitous discovery-space to a more principled survey that is specifically designed to study these features.

In this article, we introduce a new survey that moves in this direction. The Disk Substructures at High Angular Resolution Project (DSHARP) was conducted as one of the first Large Programs with the Atacama Large Millimeter/submillimeter Array (ALMA). DSHARP aims to measure the 240 GHz continuum emission at ~ 35 mas (5 au) resolution for 20 nearby disks as part of an effort to better understand the evolution of solid particles during the planet formation process. Having motivated the project above, this article also describes the DSHARP survey design and sample (Section 2), the ALMA observations (Section 3) and their calibration (Section 4), and some basic observational results (Section 5). We conclude with the DSHARP data release (Section 6) and a broad overview of a series of accompanying articles that highlight some initial results (Section 7).

2. SURVEY DESIGN AND SAMPLE

The DSHARP survey design tried to optimize a combination of spatial resolution and emission contrast sensitivity. We defined two criteria to guide that design, based on theoretical expectations for the origins of substructures and the observational limits that ALMA imposed at the time of proposing (2016 April).

The first criterion was access to a reasonable range of spatial scales down to a resolution of 6 au (or better). Such high resolution was essential for identifying the continuum substructures found in the sharpest ALMA disk images available at the time (ALMA Partnership et al. 2015; Andrews et al. 2016). Moreover, it is comparable to the typical (disk-averaged) gas pressure scale height, H (where $H/r \approx 0.1$), a benchmark size that can be directly related to the pressure deviations generated by turbulent zonal flows (e.g., Johansen et al. 2009), vortices (e.g., Barge & Sommeria 1995), or the gaps opened by nascent planets (e.g., Lin & Papaloizou 1993). At a resolution of ~ 6 au, H -sized features in radius or azimuth would be resolved in the outer disk, and should be detectable at $r \approx 10$ au (for sufficient contrast).

The second criterion was the ability to detect a brightness perturbation with a contrast of $\sim 10\%$ out to scales comparable to the planetary orbits in the solar system ($r \approx 40$ au). This is roughly the contrast measured for the weaker substructures in the HL Tau and TW Hya disks (e.g., Akiyama et al. 2016; Huang et al. 2018b). It is also sufficient to detect the $\sim 20\%$ pressure variations produced by $\gtrsim 0.1 M_{\text{Jup}}$ planets (Fung et al. 2014), zonal flows (Simon & Armitage 2014), or weak vortices (e.g., Goodman et al. 1987), even if (contrary to expectations) there is no accompanying concentration of the solids (presuming the emission is optically thin).

The combination of these criteria and ALMA technical restrictions meant that the optimal observing frequency was in the vicinity of 240 GHz (Band 6). Higher frequency observations at comparable (or better) resolution were not permitted for Cycle 4 Large Programs (these were a “non-standard” mode of observation), and the resolution and sensitivity options at lower frequencies were both insufficient for our goals.

The resolution criterion drove the practical planning for the survey sample. The ALMA Cycle 4 array configuration schedule was set to provide the requisite high angular resolution (configurations C40-8 and C40-9, with maximum baseline lengths of 6.8–12.6 km) during 2017 June and July.¹ We therefore started building a sample by targeting disks that are sufficiently nearby to give the required spatial resolution for those configurations ($d < 200$ pc), and that transit at high elevations at night during this time period. Those criteria limited the sample to targets in the Ophiuchus (Wilking et al. 2008), Lupus (Comerón 2008), and Upper Scorpius (Preibisch & Mamajek 2008) regions, along with a few isolated targets. We further narrowed the field by focusing on Class II sources, to remove any ambiguity associated with circumstellar envelopes. We also excluded previously-identified “transition” disks, since they are already known to exhibit substructure (by definition) and the emphasis here is on assessing the prevalence of substructures in the general disk population.

Those criteria still leave ~ 200 potentially viable targets. A more severe cut was made on sensitivity considerations, in an effort to meet the contrast criterion. As it was stated above, that criterion is vague. Being more specific is somewhat arbitrary, but we chose some fiducial numbers to guide the strategy. For a target at $d = 140$ pc and a synthesized beam FWHM of 45 mas, we aimed to achieve a noise level sufficient for measuring (at $\text{SNR} = 2$) a 10% deviation from an otherwise smooth brightness profile at $r = 0''.3$ (~ 40 au). We selected appropriate targets for this metric based on previous continuum observations at modest ($\sim 0''.3$) resolution (e.g., Andrews et al. 2009, 2010; Ansdell et al. 2016; Barenfeld et al. 2016). For reasonable assumptions about the shape of the brightness profile,² this criterion can be met with a cut on the $0''.3$ peak brightness for a given noise at 45 mas resolution. Some experimentation suggested a noise level objective of $17 \mu\text{Jy}$ per 45 mas beam (0.18 K)³, which limits us to targets with peak

¹ See the Cycle 4 Proposer’s Guide, <https://almascience.eso.org/documents-and-tools/cycle4/alma-proposers-guide>, Table 3.

² We assumed that $I_\nu \propto r^{-0.5} - r^{-1}$. At the time, there was scant published evidence to support (or refute) such profile shapes, but it has since been shown that this is appropriate (e.g., see Tripathi et al. 2017; Andrews et al. 2018). We conservatively assumed a face-on orientation in setting this benchmark.

³ Unless specified otherwise, DSHARP brightness temperatures are calculated assuming the standard Rayleigh-Jeans relation.

Table 1. DSHARP Host Star and Accretion Properties

Name	Region	ϖ /mas	d /pc	SpT	$\log T_{\text{eff}}$ /K	$\log L_*/L_{\odot}$	$\log M_*/M_{\odot}$	$\log t_*/\text{yr}$	$\log \dot{M}_*/M_{\odot} \text{ yr}^{-1}$	Refs.
(1)	(2)	(3)	(4)	(5)	(6)	(7)	(8)	(9)	(10)	(11)
HT Lup ^a	Lup I	6.49 ± 0.06	154 ± 2	K2	3.69 ± 0.02	0.74 ± 0.20	$0.23^{+0.06}_{-0.13}$	5.9 ± 0.3	< -8.4	1, 1, 1
GW Lup	Lup I	6.42 ± 0.06	155 ± 3	M1.5	3.56 ± 0.02	-0.48 ± 0.20	$-0.34^{+0.10}_{-0.17}$	6.3 ± 0.4	-9.0 ± 0.4	1, 1, 1
IM Lup	Lup II	6.31 ± 0.05	158 ± 3	K5	3.63 ± 0.03	0.41 ± 0.20	$-0.05^{+0.09}_{-0.13}$	5.7 ± 0.4	-7.9 ± 0.4	1, 1, 1
RU Lup	Lup II	6.27 ± 0.07	159 ± 3	K7	3.61 ± 0.02	0.16 ± 0.20	$-0.20^{+0.12}_{-0.11}$	5.7 ± 0.4	-7.1 ± 0.3	1, 1, 1
Sz 114	Lup III	6.16 ± 0.05	162 ± 3	M5	3.50 ± 0.01	-0.69 ± 0.20	$-0.76^{+0.08}_{-0.07}$	$6.0^{+0.1}_{-0.8}$	-9.1 ± 0.3	1, 1, 1
Sz 129	Lup IV	6.19 ± 0.05	161 ± 3	K7	3.61 ± 0.02	-0.36 ± 0.20	$-0.08^{+0.03}_{-0.15}$	6.6 ± 0.4	-8.3 ± 0.3	1, 1, 1
MY Lup ^b	Lup IV	6.39 ± 0.05	156 ± 3	K0	3.71 ± 0.02	-0.06 ± 0.20	$0.09^{+0.03}_{-0.13}$	$7.0^{+0.6}_{-0.3}$	< -9.6	1, 1, 1
HD 142666	Upper Sco	6.74 ± 0.05	148 ± 2	A8	3.88 ± 0.02	0.96 ± 0.21	$0.20^{+0.04}_{-0.01}$	7.1 ± 0.3	< -8.4	2, 2, 2
HD 143006	Upper Sco	6.02 ± 0.15	165 ± 5	G7	3.75 ± 0.02	0.58 ± 0.15	$0.25^{+0.05}_{-0.08}$	6.6 ± 0.3	-8.1 ± 0.4	3, 4, 5
AS 205 ^c	Upper Sco	7.82 ± 0.10	128 ± 2	K5	3.63 ± 0.03	0.33 ± 0.15	$-0.06^{+0.07}_{-0.05}$	5.8 ± 0.3	-7.4 ± 0.4	3, 4, 6
SR 4	Oph L1688	7.43 ± 0.05	134 ± 2	K7	3.61 ± 0.02	0.07 ± 0.20	$-0.17^{+0.11}_{-0.14}$	5.9 ± 0.4	-6.9 ± 0.5	7, 8, 9
Elias 20	Oph L1688	7.22 ± 0.23	138 ± 5	M0	3.59 ± 0.03	0.35 ± 0.20	$-0.32^{+0.12}_{-0.07}$	< 5.9	-6.9 ± 0.5	9, 8, 9
DoAr 25	Oph L1688	7.22 ± 0.08	138 ± 3	K5	3.63 ± 0.03	-0.02 ± 0.20	$-0.02^{+0.04}_{-0.19}$	6.3 ± 0.4	-8.3 ± 0.5	10, 11, 12
Elias 24	Oph L1688	7.34 ± 0.11	136 ± 3	K5	3.63 ± 0.03	0.78 ± 0.20	$-0.11^{+0.16}_{-0.08}$	5.3 ± 0.4	-6.4 ± 0.5	10, 8, 9
Elias 27	Oph L1688	8.63 ± 0.98	116^{+19}_{-10}	M0	3.59 ± 0.03	-0.04 ± 0.23	$-0.31^{+0.15}_{-0.11}$	5.9 ± 0.5	-7.2 ± 0.5	7, 11, 9
DoAr 33	Oph L1688	7.15 ± 0.06	139 ± 2	K4	3.65 ± 0.03	0.18 ± 0.20	$0.04^{+0.05}_{-0.17}$	6.2 ± 0.4	...	13, 8
WSB 52	Oph L1688	7.30 ± 0.09	136 ± 3	M1	3.57 ± 0.03	-0.15 ± 0.20	$-0.32^{+0.13}_{-0.17}$	5.8 ± 0.5	-7.6 ± 0.5	7, 8, 9
WaOph 6	Oph N 3a	8.07 ± 0.05	123 ± 2	K6	3.62 ± 0.03	0.46 ± 0.20	$-0.17^{+0.17}_{-0.09}$	5.5 ± 0.5	-6.6 ± 0.5	14, 11, 14
AS 209	Oph N 3a	8.27 ± 0.06	121 ± 2	K5	3.63 ± 0.03	0.15 ± 0.20	$-0.08^{+0.11}_{-0.14}$	6.0 ± 0.4	-7.3 ± 0.5	15, 11, 6
HD 163296	isolated?	9.85 ± 0.11	101 ± 2	A1	3.97 ± 0.03	1.23 ± 0.30	$0.31^{+0.05}_{-0.03}$	7.1 ± 0.6	-7.4 ± 0.3	2, 2, 2

^a HT Lup (Sz 68) is a triple system: the primary has a close ($0''.1$) and faint ($\Delta K \approx 6$) companion as well as a more distant ($2''.8$) and even fainter ($\Delta K \approx 10$) tertiary (Ghez et al. 1997). The observations used to estimate the parameters here are from the combined light of the central pair, but should be dominated by (and therefore representative of) the primary. See Troncoso et al. (2018) for more details.

^b The MY Lup disk is sufficiently inclined and flared that it likely is a source of self-extinction. The derived L_* (and thereby t_*) is likely unrealistically low (and the age too old). See Huang et al. (2018a) or Weaver et al. (2018) for more details.

^c AS 205 (V866 Sco) is also a triple system: the primary is separated from the secondary by $1''.3$ (Ghez et al. 1993), and the secondary is itself a spectroscopic binary (Eisner et al. 2005). The host parameters listed here are for the primary only. See Troncoso et al. (2018) for more details.

NOTE—Col. (1) Target name. Col. (2) Associated star-forming region. The Lupus sub-cloud regions are as designated by Cambrésy (1999). Upper Sco memberships were made following Luhman et al. (2018). AS 209 and WaOph 6 are located well northeast of the main Oph region in the Oph N 3a complex. They are most closely associated with the L163 and L162 dark clouds, respectively. Col. (3) Parallax measurement from *Gaia* DR2 (Gaia Collaboration et al. 2018). Col. (4) Distance (computed from Col. 3). Col. (5) Spectral type from the literature (see the first reference entries in Col. 11). Col. (6) Effective temperatures from the literature, scaled according to the appropriate d in Col. (4) (see second reference entries in Col. 11). Cols. (8)+(9) Stellar masses and ages, inferred from $\{T_{\text{eff}}, L_*\}$ and MIST evolutionary models (Choi et al. 2016) as described by Andrews et al. (2018). Col. (9) Accretion rates, inferred from (properly scaled) accretion luminosities (see the third reference entries in Col. 11) as described by Andrews et al. (2018). All quoted measurements correspond to the peak of the marginalized posterior distributions. Uncertainties reflect the 68.3% confidence interval; limits are taken at the 95.5% confidence level. Col. (11): Reference for the quoted SpT, $\{T_{\text{eff}}, L_*\}$, and accretion luminosity measurements: 1 = Alcalá et al. (2017), 2 = Fairlamb et al. (2015), 3 = Luhman & Mamajek (2012), 4 = Barenfeld et al. (2016), 5 = Rigliaco et al. (2015), 6 = Salyk et al. (2013), 7 = Luhman & Rieke (1999), 8 = Andrews et al. (2010), 9 = Natta et al. (2006), 10 = Wilking et al. (2005), 11 = Andrews et al. (2009), 12 = Muzerolle et al. (1998), 13 = Bouvier & Appenzeller (1992), 14 = Eisner et al. (2005), 15 = Herbig & Bell (1988).

brightness $I_{\nu} \gtrsim 20$ mJy per $0''.3$ beam (4.8 K). The key caveat is that most of the available data at $0''.3$ resolution were taken at 340 GHz; in those cases, we assumed that $I_{\nu} \propto \nu^{2.5}$ (cf., Andrews & Williams 2005).

While that brightness cut substantially limits the pool of potential targets, the sample size was ultimately set by ALMA timeshare restrictions. Only ~ 30 hours in the LST ranges of interest were set aside for Large Programs in each of the two extended array configurations. The desired noise could be reached in ~ 1 hour of integration per target, but the factor of three overhead costs meant that the sample size was limited to 10 targets per configuration. We selected 10 targets (mostly in Oph) for the more compact of the two offered configurations (C40-8,

up to 7.8 km baselines; 50 mas resolution), based on their nominally closer distances (125 pc; de Geus et al. 1989; Loinard et al. 2008). An additional 10 targets (primarily in Lup) were chosen for the C40-9 configuration (up to 12.6 km baselines; 35 mas resolution).

The sample of 20 targets resulting from this selection process spans a broad parameter-space. The stellar host properties are compiled in Table 1. Distance (d) estimates⁴ were derived from *Gaia* DR2 parallax mea-

⁴ Note that the $d = 125$ pc used to motivate the slightly coarser resolution for Oph targets was inappropriate. However, Section 3 discusses how this aspect of the survey design was ignored due to unforeseen alterations in the configuration schedule.

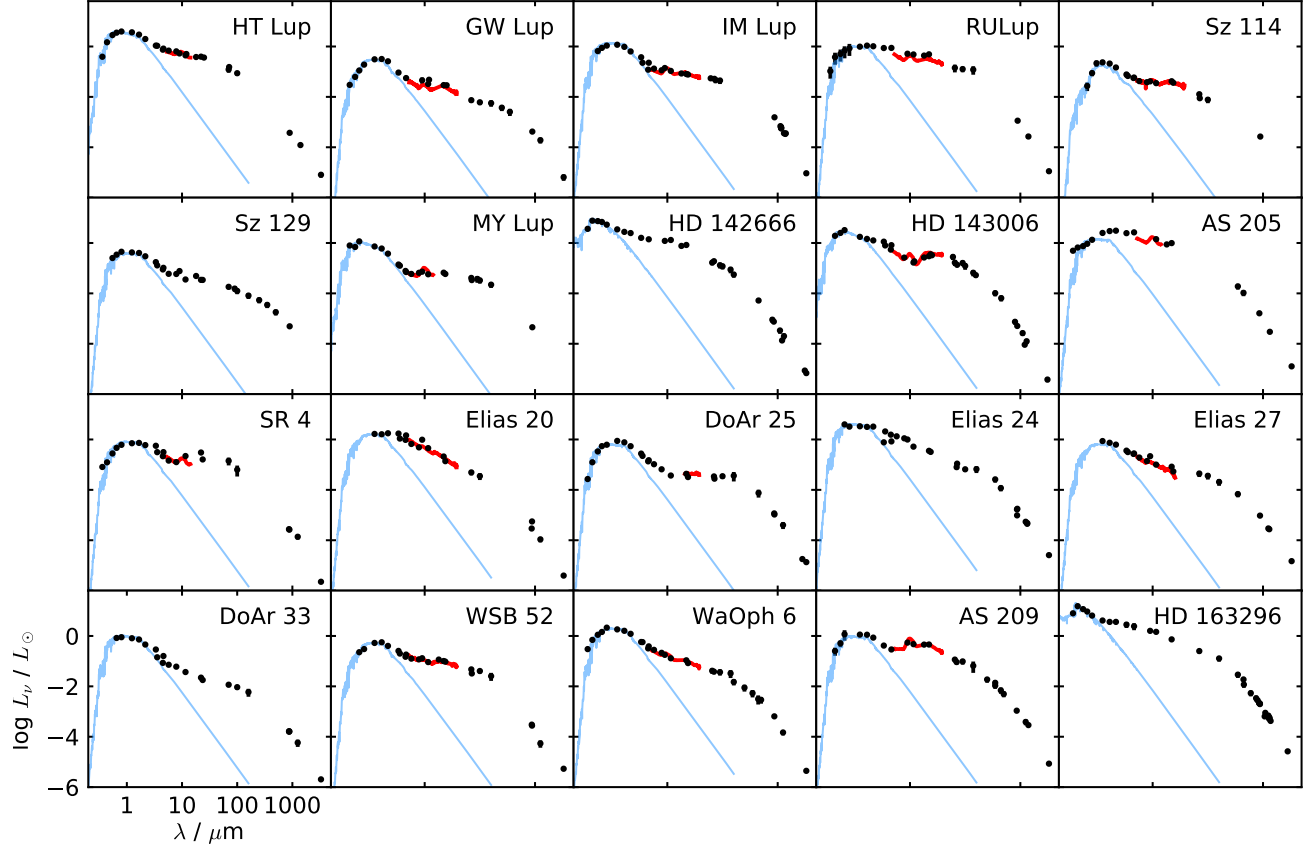


Figure 1. Broadband SEDs for the sample targets, compiled from the literature. Note the ordinate axis is $L_\nu = 4\pi d^2 \nu F_\nu$ in L_\odot units. These SEDs have been de-reddened using the extinction values quoted by the references listed in Col. (11) of Table 1 (second entries) and the prescription described by Andrews et al. (2013). Blue curves represent the NEXTGEN/BT-settl photosphere models (Allard et al. 2003, 2011) corresponding to the stellar parameters listed in Table 1. Red curves show the *Spitzer* IRS spectra available from the Infrared Science Archive (IRSA). Note that the SEDs for HT Lup and AS 205 include contributions from multiple individual components. Optical photometry was collected from a range of sources (Vrba et al. 1993; Herbst et al. 1994; Hughes et al. 1994; Oudmaijer et al. 2001; Wilking et al. 2005; Gras-Velázquez & Ray 2005; Eisner et al. 2005; Padgett et al. 2006; Grankin et al. 2007; Merín et al. 2008; Mendigutía et al. 2012); infrared measurements were culled from 2MASS (Skrutskie et al. 2006), WISE (Wright et al. 2010), *Spitzer* imaging surveys (Carpenter et al. 2008; Evans et al. 2009), AKARI (Ishihara et al. 2010), and *Herschel* far-infrared measurements at IRSA; measurements at (sub-)mm wavelengths come from various sources (Andre & Montmerle 1994; Mannings & Emerson 1994; Sylvester et al. 1996; Nuernberger et al. 1997; Mannings & Sargent 1997; Dent et al. 1998; Henning et al. 1998; Natta et al. 2004; Stanke et al. 2006; Andrews & Williams 2007; Lommen et al. 2007, 2009; Roccatagliata et al. 2009; Andrews et al. 2009; Isella et al. 2007; Pinte et al. 2008; Isella et al. 2009; Ricci et al. 2010; Sandell et al. 2011; Öberg et al. 2011; Pérez et al. 2012, 2015; Qi et al. 2015; Ansdell et al. 2016; Cleeves et al. 2016; Barenfeld et al. 2016; Ubach et al. 2017; Huang et al. 2017; Tripathi et al. 2017; Cox et al. 2017; Andrews et al. 2018). These SEDs are available in a set of ASCII files (an associated readme file explains their format) as part of the Supplementary Data associated with this article.

surements (Gaia Collaboration et al. 2018), following Astraatmadja & Bailer-Jones (2016) for a flat d prior. Literature estimates of the effective temperatures (T_{eff}) and luminosities (L_* ; re-scaled for the appropriate d) were adopted to derive masses (M_*) and ages (t_*) based on the MIST stellar evolution models (Choi et al. 2016), following the methodology described by Andrews et al. (2018). Accretion rates (\dot{M}_*) were calculated from those host parameters and measurements of accretion luminosities (scaled for d) in the literature (see the Table 1 notes). The sample hosts exhibit the full range of young star properties, with $M_* \approx 0.2\text{--}2 M_\odot$ and nearly two

decades spanned in both L_* and \dot{M}_* . The mean age in the sample is 1 Myr, although with considerable individual uncertainties (and of course various untreated systematics; see Soderblom et al. 2014).

Despite the range of these properties, the sample hosts are not quite representative of a *typical* young star: they tend to have earlier spectral types, and are accordingly more massive, luminous, and accreting more vigorously than stars at the peak of the initial mass function. This selection bias enters implicitly with the sensitivity criterion, since we required a previous measurement at modest resolution. The datasets from which those measure-

Table 2. DSHARP Observing Log (ALMA Program 2016.1.00484.L)

Name	UTC Date	Config.	Baselines	N_{ant}	$\mathcal{E}/^{\circ}$	PWV/mm	Calibrators
(1)	(2)	(3)	(4)	(5)	(6)	(7)	(8)
HT Lup	2017/05/14-04:11	C40-5	15 m – 1.1 km	43	76–77	1.00–1.15	J1517-2422, J1427-4206, J1610-3958, J1540-3906
	2017/05/17-02:12	C40-5	15 m – 1.1 km	49	58–67	0.90–1.05	J1517-2422, J1517-2422, J1610-3958, J1540-3906
	2017/09/24-17:39	C40-8/9	41 m – 12.1 km	39	59–70	0.60–1.15	J1517-2422, J1517-2422, J1534-3526, J1536-3151
	2017/09/24-19:12	C40-8/9	41 m – 12.1 km	39	75–78	0.65–1.05	J1517-2422, J1427-4206, J1534-3526, J1536-3151
GW Lup	2017/05/14-04:11	C40-5	15 m – 1.1 km	43	69–72	1.00–1.15	J1517-2422, J1427-4206, J1610-3958, J1540-3906
	2017/05/17-02:12	C40-5	15 m – 1.1 km	49	51–61	0.90–1.05	J1517-2422, J1517-2422, J1610-3958, J1540-3906
	2017/09/24-23:31	C40-8/9	41 m – 14.9 km	40	29–39	0.80–1.20	J1617-5848, J1733-1304, J1534-3526, J1536-3151
	2017/11/04-14:59	C43-9	113 m – 13.9 km	43	58–69	0.60–0.80	J1427-4206, J1427-4206, J1534-3526, J1536-3151

NOTE—Basic information from the individual execution blocks conducted as part of ALMA Program 2016.1.00484.L. Col. (1) Target name. Col. (2) UTC date and time for the start of the execution block. Col. (3) ALMA configuration. Col. (4) Minimum and maximum baseline lengths. Col. (5) Number of antennas available. Col. (6) Target elevation range. Col. (7) Range of precipitable water vapor levels. Col. (8) From left to right, the quasars observed for calibrating the bandpass, amplitude scale, phase variations, and checking the phase transfer. Additional archival observations used in our analysis are compiled in Table 3. Table 2 is published in its entirety in the electronic edition of the journal. A portion is shown here for guidance regarding its form and content. (*The full table is appended for review.*)

ments were drawn are biased toward brighter continuum sources, which then permeates to the host properties since the continuum luminosity scales steeply with M_* (Andrews et al. 2013; Mohanty et al. 2013) and \dot{M}_* (Manara et al. 2016; Mulders et al. 2017). Unfortunately, this was an unavoidable limitation at the time of planning the program. Since then, ALMA continuum surveys at suitable resolution have been conducted that could aid in reducing future bias (e.g., Ansdel et al. 2016; Pascucci et al. 2016; Barenfeld et al. 2016).

Figure 1 shows a gallery of the spectral energy distributions (SEDs) for the sample targets. These SEDs are typical for Class II disks, in that they are have a morphology that is consistent with the median SEDs computed from larger samples of similar targets (e.g., Ribas et al. 2017). According to such aggregations, the SEDs for RU Lup, AS 205, and AS 209 are in the top quartile of Class II sources (i.e., are over-luminous); the SEDs for HD 143006, SR 4, and DoAr 25 are relatively low in the near-infrared and high in the far-infrared (similar to, though not nearly as pronounced as, the typical transition disk SED); and the SEDs for DoAr 33 and WaOph 6 are in the bottom quartile for Class II sources. Coupled with the range of stellar host properties, this diversity in SED behavior provides a basis for exploring how the resolved emission distributions vary with some of the key “bulk” parameters that are used in larger demographic studies of the general disk population.

3. OBSERVATIONS

The observations for this project were conducted from 2017 May to November as part of ALMA program 2016.1.00484.L. All measurements used the ALMA Band 6 receivers and correlated four spectral windows (SPWs) in dual polarization mode. Three SPWs were set in time-division mode (TDM), centered at 232.6, 245.0, and 246.9 GHz, with each sampling the continuum in 128 channels spanning 1.875 GHz (31.25 MHz

per channel). The remaining SPW was set in frequency-division mode (FDM), centered at the $^{12}\text{CO } J=2-1$ rest frequency (230.538 GHz), and covering a bandwidth of 937.5 MHz in 3840 channels (488.281 kHz channel spacing, 0.635 km s^{-1} velocity resolution). The plan was to observe each target briefly in the C40-5 (hereafter “compact”) configuration, and also for ~ 1 hour in the C40-8 or C40-9 (hereafter “extended”) configurations. The actual observing log is provided in Table 2.

The compact configuration observations employed an array with baseline lengths from 15 m to 1.1 km (corresponding to a resolution of $\sim 0''.23$ and a maximum recoverable scale of $\sim 2''.6$). These observations shared execution blocks among nearby targets, and were conducted to provide 12 minutes of integration time per source. The observations cycled between the targets and a nearby phase calibrator on a 6 minute cycle; an additional “check” phase calibrator (to assess the quality of phase transfer) was observed every 30 minutes. A bandpass and amplitude calibrator (sometimes the same quasar) were observed during each execution block. The log in Table 2 includes information about the observing conditions and identifies the calibration sources.

We relied on archival ALMA Band 6 observations of 5 targets (IM Lup, HD 142666, Elias 24, Elias 27, HD 163296) rather than obtain new C40-5 data, and folded in additional archival data for three other targets (HD 143006, AS 205, AS 209). Some information about these supplementary datasets are compiled in Table 3. The spectral setups, observing strategies, and weather conditions are described in the listed references (Col. 8).

The extended (C40-8 and C40-9) configuration observations deviated substantially from the survey design outlined in Section 2. The Atacama desert was hit with two major winter storms in short succession just before the planned antenna moves to the C40-9 configuration, covering the ALMA site with two meters of snow and effectively halting operations for about a month. By

Table 3. Archival ALMA Datasets

Name	UTC Date	Config.	Baselines	N_{ant}	Calibrators	Program	Refs.
(1)	(2)	(3)	(4)	(5)	(6)	(7)	(8)
IM Lup	2014/07/06-22:18	C34-4	20 – 650 m	31	J1427-4206, Titan, J1534-3526, J1626-2951	2013.1.00226.S	1
	2014/07/17-01:38	C34-4	20 – 650 m	32	J1427-4206, Titan, J1534-3526, ...	2013.1.00226.S	1
	2015/01/29-09:48	C34-2/1	15 – 349 m	40	J1517-2422, Titan, J1610-3958, ...	2013.1.00694.S	2
	2015/05/13-08:30	C34-3/4	21 – 558 m	36	J1517-2422, Titan, J1610-3958, ...	2013.1.00694.S	2
	2015/06/09-23:42	C34-5	21 – 784 m	37	J1517-2422, Titan, J1610-3958, J1614-3543	2013.1.00798.S	3
HD 142666	2015/07/21-22:27	C34-7/6	15 – 1600 m	44	J1517-2422, Titan, J1627-2426, J1625-2527	2013.1.00498.S	...

NOTE—Col. (1) Target name. Col. (2) UTC date and time for the start of the execution block. Col. (3) ALMA configuration. Col. (4) Range of baseline lengths. Col. (5) Number of antennas available. Col. (6) From left to right, the quasars observed for calibrating the bandpass, amplitude scale, phase variations, and checking the phase transfer. Col. (7) ALMA program ID number. Col. (8) Published references: 1 = Huang et al. (2017), 2 = Cleeves et al. (2016), 3 = Pinte et al. (2018), 4 = Salyk et al. (2014), 5 = Dipierro et al. (2018), 6 = Pérez et al. (2016), 7 = Fedele et al. (2018), 8 = Flaherty et al. (2015), 9 = Isella et al. (2016). Table 3 is published in its entirety in the electronic edition of the journal. A portion is shown here for guidance regarding its form and content. (*The full table is appended for review.*)

the time the snow was cleared enough to start observations in the C40-8 configuration, it was early September (rather than early June), and our targets were setting in the early evening. The strategy was adjusted to optimize for completion: we abandoned the assignment of targets to specific array configurations and were granted permission to observe in the C43-10 configuration at the start of Cycle 5 (2017 October). The observations continued in the C43-9 and C43-8 configurations throughout October and November (in the latter case, catching the targets as they rose in the mornings).

Fortunately, despite the less-than-optimal scheduling, nearly all of the targets were observed for two executions (often in different configurations) in conditions with excellent phase stability, each with \sim 35 minutes of on-source integration time.⁵ Sz 114, AS 205, and DoAr 25 each had only a single successful execution. The spectral setup was the same as for the compact configuration observations. Observations cycled between a single science target and a nearby phase calibrator on 1 minute intervals, again with a second “check” calibrator observed every 30 minutes. Standard bandpass and amplitude calibrators were observed in each execution block. The relevant information on those calibrators and the observing conditions are included in Table 2.

4. CALIBRATION

Since this survey is among the first to collect such a large volume of ALMA data using such extended baseline configurations, a substantial effort was made to explore various calibration strategies to optimize the final data quality. The standard methodology that resulting from this exploration is described in this section. The specific details on the calibration of datasets for individual targets are available from the DSHARP reposi-

tory⁶, including calibration scripts, calibrated measurement sets, images, and some additional post-processed products (see Section 6). All calibration tasks are performed with the CASA software package (McMullin et al. 2007) and a small supplement of python tasks (these are also available in the DSHARP repository).

4.1. Pipeline Calibration

The first step in this process is the standard calibration with the CASA pipeline. This procedure was performed by ALMA staff separately for the compact and extended configuration data, using CASA v4.7.2 or v5.1.1–5 for datasets that were processed before or after 2017 November, respectively. The pipeline first imports the raw data and performs some basic deterministic flagging of problematic scans, channels, or antennas. It then derives a calibration table of system temperatures (T_{sys}) and flags scans with discrepant values. For most of the data in this sample, $T_{\text{sys}} \approx 60\text{--}80$ K; in the poorest conditions it could reach \sim 130 K, and in the best cases it was as low as 50 K. Next, the visibility phases are adjusted according to measurements by the water vapor radiometer (WVR) system. For the extended configuration data, the median improvement in the RMS phase variations achieved by those corrections was a factor of \sim 1.7, although individual datasets saw improvements as small as a factor of 1.2 and as large as 3. The corrected RMS phase variations (far from the reference antenna) were typically 30° (with a sample range \sim 15– 50°). The compact configuration observations saw similar improvement factors (1.5–3.0) and (naturally) lower corrected RMS phase variations (\sim 10°).

The pipeline then performs the standard bandpass calibration, using the first quasar in the calibrator list in Table 2 as the reference. It continues by setting the amplitude scale, using measurements of the second quasar in the Table 2 list. The mean flux density in each SPW

⁵ The conditions for the 2017/09/08 and 2017/11/26 observations of the HD 163296 and HD 143006 disks limited the on-source integration times to 20 and 28 minutes, respectively.

⁶ <http://almascience.nrao.edu/alma-data/DSHARP>

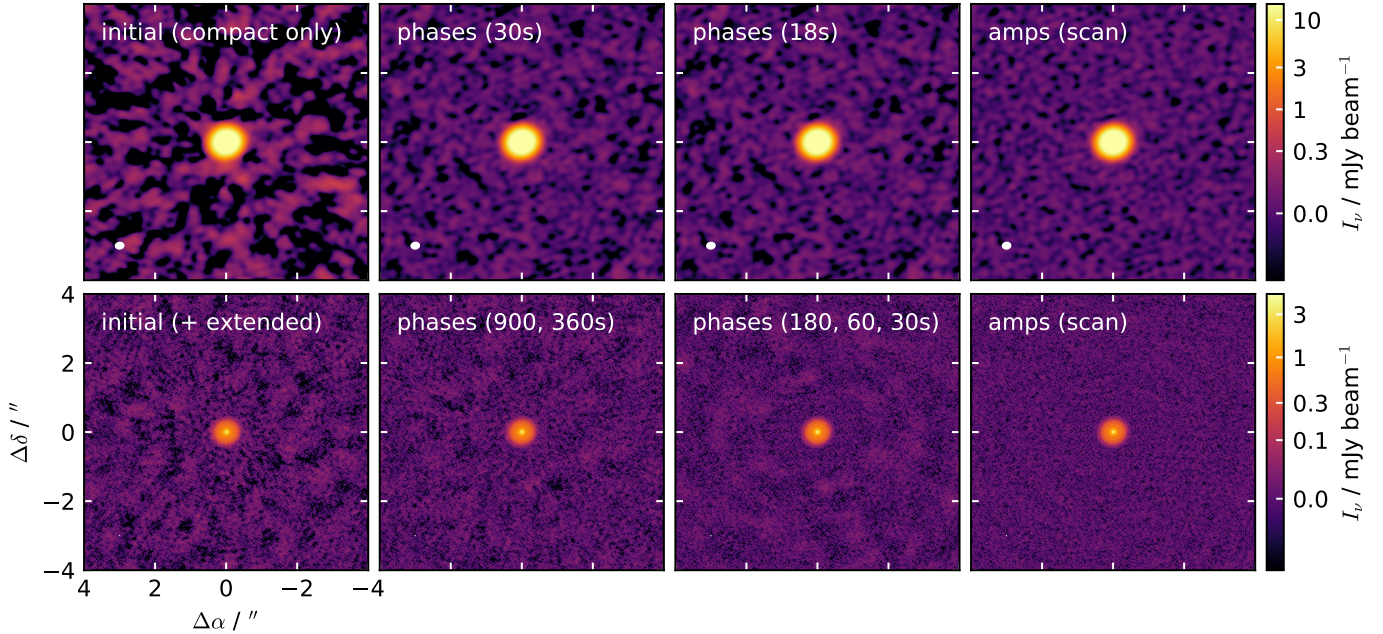


Figure 2. An illustration of self-calibration improvements for the RU Lup disk. The top panels show images along the self-calibration sequence (the type and interval are annotated) for the compact configuration (C40-5) data alone (on the same scale, saturated to accentuate the noise). The beam dimensions are shown in the lower left corner of each panel. The peak SNR increases from 555 to 2120, and the noise decreases from 110 to $30 \mu\text{Jy beam}^{-1}$ along the sequence. An analogous sequence is shown in the bottom panels, where the extended configuration (C40-8/9 + C43-8) data have been folded in (combined with the self-calibrated C40-5 data); the beam dimensions are plotted, but are too small to render clearly. The peak SNR increases from 250 to 400 and the noise decreases from 18 to $14 \mu\text{Jy beam}^{-1}$ across the sequence. Note that the `clean` mask region is visible in this intensity stretch as an approximately circular region with $\sim 1''$ radius.

for that quasar is determined from a power-law spectral model based on regular (bi-monthly) monitoring in ALMA Bands 3 and 7 (~ 100 and 340 GHz), with those measurements referenced to primary calibrators (planets or moons). The flux scale will be checked (and adjusted if necessary) in the post-processing steps outlined below. Finally, the complex gain variations with time were corrected based on measurements of the nearby quasar (third in the Table 2 calibrator list) that were interleaved with observations of the science target.

4.2. Self-Calibration

This standard pipeline calibration generally worked well for these datasets. The CASA measurement set containing the visibilities calibrated up to this point can be obtained by running the pipeline with the raw data and calibration tables available in the ALMA archive. However, creating scientifically useful data products required substantial post-processing, with particular emphasis on combining and self-calibrating the visibilities. Whenever possible, we followed a homogenized strategy that was designed specifically for that effort. This post-processing component of the calibration was conducted with CASA v5.1.0 and custom python routines.

The procedure starts with the compact configuration data. A pseudo-continuum dataset is created by flagging channels located $\pm 25 \text{ km s}^{-1}$ from the CO $J=2-1$ line center and then spectrally averaging into 125 MHz

channels. The continuum visibilities corresponding to each individual observation are imaged (Section 4.3) and then checked to ensure consistent astrometric registration and flux calibration (if necessary, they are corrected; Section 4.4). The data from the individual observations are then combined. With the combined dataset, we perform a sequence of phase-only self-calibration iterations, stepping down in a set of solution intervals $\{60, 30, 18, 6 \text{ s}\}$ (a 120 s interval is sometimes included). Reference antennas are selected based on their data quality and proximity to the array center. When possible, we do not combine the SPWs (or scans), in an effort to correct SPW-dependent gain variations. After each iteration of self-calibration, the data are again imaged. An estimate of the RMS noise is made in an annular region, within a $4''25$ -radius circle centered on the target but excluding the image mask. The phase self-calibration sequence is stopped after either reaching a solution interval on the record length (6 s) or if the peak SNR does not appreciably change (decreases by $< 5\%$). Finally, we perform a single iteration of amplitude self-calibration on a scan-length interval (~ 6 minutes for DSHARP data).

For the DSHARP observations in the C40-5 configuration, the self-calibration procedure outlined above provides a dramatic improvement in data quality. The top panels of Figure 2 illustrate this for a representative case. The peak SNR increased by a factor of three, resulting in a typical RMS noise of $30 \mu\text{Jy beam}^{-1}$ for a

$\text{FWHM} = 0''.27 \times 0''.23$ beam (10 mK). The same procedure was applied in the cases that included archival datasets, leading to similar improvements.

The next step is to prepare the extended configuration datasets. To again make a pseudo-continuum, the channels corresponding to the same velocity range around the CO line as for the compact configuration datasets were flagged, and then the data were averaged into 125 MHz channels and 6 s integrations (these data were recorded with 2 s integrations). The data for each individual observation were imaged and then checked for center misalignments and any flux calibration discrepancies. Once those are corrected (if necessary), the compact and extended configuration visibilities were combined.

The phases for the combined dataset were iteratively self-calibrated on solution intervals of $\{900, 360, 180, 60, 30, 6 \text{ s}\}$ (usually only $\{180, 60, 30 \text{ s}\}$ are necessary). The individual SPWs were combined in this case to enhance the SNR on longer baselines. For antenna pairings with $\text{SNR} \leq 1.5$ on these intervals, the self-calibration solutions were not applied but the corresponding data were not flagged (`applymode='calonly'` in the `applycal` task). The sequence is stopped when the peak SNR does not increase by $> 5\%$ and the map quality does not visually improve. One iteration of amplitude self-calibration is then attempted on the interval used at the start of the phase self-calibration sequence.

For the combined datasets, this self-calibration results in a typical improvement of 40% in the peak SNR, although in some cases there is little change and in others there is a much larger benefit. The bottom panels of Figure 2 illustrate a typical self-calibration sequence. The differences are generally smaller here because the compact configuration data were already self-calibrated and the extended configuration data were taken in excellent conditions. The typical RMS noise level measured in the combined, self-calibrated datasets is $13 \mu\text{Jy}$ per $\sim 40 \text{ mas beam}$ (0.17 K), roughly 30% better than was specified in the survey design strategy.

Once the continuum self-calibration is satisfactory, the same gain tables are applied to the non-spectrally-averaged visibilities (after any required astrometric and flux calibration adjustments) to obtain a corresponding calibrated measurement set for the region of the spectrum around the CO $J=2-1$ emission line.

4.3. Imaging During Self-Calibration

Self-calibration relies on continuum emission models assembled from the ‘clean’ components derived from interferometric imaging. We adopted a set of imaging standards in an effort to homogenize the calibration effort. All imaging was performed with the `tclean` task in `CASA v5.1.0`. For the self-calibration of the compact configuration data, we imaged out to the FWHM of the primary beam ($\theta_{\text{pb}} = 26''$) with 30 mas pixels (~ 10 per synthesized beam FWHM, θ_b) to check for any problematic background sources. Finding none, the

self-calibration of the combined datasets used $9''$ -wide images with 3 mas pixels (again, ~ 10 pixels per θ_b).

We employed the `tclean` multi-scale, multi-frequency synthesis deconvolution mode (Cornwell 2008) with a Briggs `robust=0.5` weighting scheme. Simple elliptical clean masks that reflect the bulk target emission geometry (aspect ratio, position angle) and safely pad the outer reaches of the emission distribution were used. The adopted (Gaussian) deconvolution scales are target-dependent, but always include a point-like contribution and scales comparable to θ_b and $2-3 \times \theta_b$; additional larger scales (increasing by factors of 2–3) could be selected up to the radius of the mask. The algorithm was halted on thresholds; $3 \times$ the noise early in the self-calibration sequence, and $2 \times$ the noise for the last phases-only step and amplitude self-calibration.

These adopted imaging standards during the self-calibration process were informed by considerable experimentation with the associated parameter choices. We specifically explored alternative sets of deconvolution scales, clean thresholds, masks, and pixel sizes and found that reasonable other options had negligible influence on the end products of self-calibration.

Special effort was made to verify that artifacts in the point spread function (PSF, or ‘dirty’ beam) do not corrupt the self-calibration. The extended ALMA configurations place antennas on longer baselines along three distinct arms (set by the site topography). The corresponding spatial frequency coverage can generate complicated PSF structure, sometimes with 30% sidelobe features. Figure 3 illustrates the impact, showing the connections between the sampling function (u, v coverage), PSF, and image for different array configurations and visibility weighting schemes in a representative example. We vetted the effects of those PSF structures on self-calibration by repeating the process for different combinations of visibility weighting schemes and tapers. Coupling lower `robust` values with tapers can mitigate PSF artifacts while maintaining the resolution, but at a substantial SNR cost. Direct comparisons (of both visibilities and images) between these variants and the standard methodology outlined above demonstrated that the PSF structure had negligible quantitative or qualitative impact on the self-calibration.⁷

4.4. Astrometric and Flux Scale Alignment

For about half the sample, we identified clear spatial shifts between the emission distributions in different observations of a given target. For the larger of these shifts, the cause is the source proper motion (especially relevant when folding in archival observations); in the other

⁷ The HD 163296 disk is the one exception (albeit a quite modest one): we find $\sim 10\%$ SNR improvements (relative to the standard) when self-calibration is conducted for images with `robust=0.5`, due to the combination of the target emission distribution and the unusual spatial frequency coverage from the archival data.

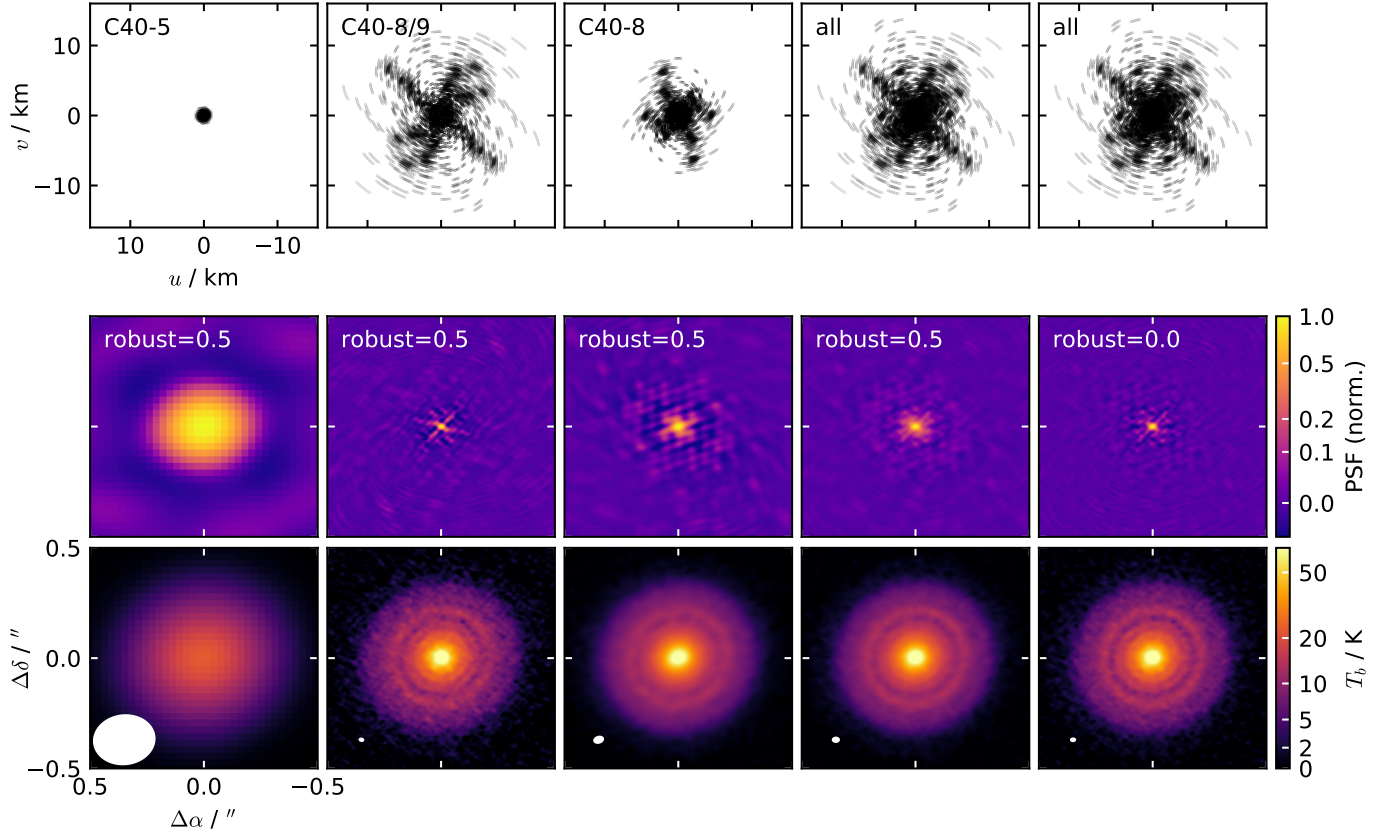


Figure 3. Illustration of the effects of spatial frequency coverage and visibility weighting on PSF structure and image morphology, again for the RU Lup disk. The top panels show the observed u,v coverage. The middle panels show the corresponding PSF structures, annotated with the corresponding `robust` weighting parameter. The bottom panels show the corresponding images, on the same T_b scale, created from subsets of the end product of the self-calibration. FWHM beam dimensions are marked in the lower left corners of each image.

cases, small (10–30 mas) mismatches are attributed to instrumental or atmospheric artifacts. Combining these datasets without correcting for their relative astrometric shifts creates a blurred (or even double) image, which is problematic when used as an initial model for self-calibration. The solution is to simply adjust the visibility phases to shift the measurements into alignment. We measure emission centroids with Gaussian peak fits in the image plane for each individual observation, and calculate the offsets relative to the highest quality extended configuration dataset. The `fixvis` task is then used to implement the appropriate phase adjustments. In cases where the observations have different pointing centers (i.e., when combining with archival data), we manually reconcile the centers using the `fixplanets` task.⁸

We routinely found slight mismatches in the amplitude scales among observations of the same target. These also need to be corrected to optimize the ini-

tial self-calibration model. Our experimentation showed that we achieved noticeably improved self-calibration results if the relative flux scale offsets between observations were $<5\%$. To quantify those mismatches, we inspected the deprojected (according to the Gaussian fit geometries noted above), azimuthally-averaged visibilities from different datasets on their overlapping baseline lengths, usually 200–500 $\text{k}\lambda$ (at lower spatial frequencies, the extended configuration data are too sparse, and at higher frequencies the averages are more strongly affected by low SNR and phase noise). Three possible outcomes from this comparison, in order of decreasing occurrence, are: (A) an offset by a roughly constant factor; (B) a mismatch that varies with spatial frequency; or (C) reasonable agreement (within 5%), and the calibration can proceed with no intervention.

In the few instances of scenario (B), we first perform an iteration of self-calibration on the phases and check the results again. The spatial frequency-dependent behavior is then alleviated, and the situation reverts to scenario (A) or (C). In scenario (A), the issue is flux calibration. The estimated ALMA flux calibration accuracy is $\sim 10\%$ for Band 6 data, although there is some uncertainty associated with that number given the adopted

⁸ To our knowledge, there is no stand-alone `CASA` routine for such astrometric corrections, though they will become more relevant with increased archive use. To align data with different pointing centers, one must first convert from the ICRS to J2000 equatorial reference frames for `fixplanets` to function properly.

Table 4. DSHARP Fiducial Continuum Image Properties

Name	ν	θ_b , PA _b	robust	θ_{tap} , PA _{tap}	RMS noise	peak I_{ν} , T_b	F_{ν}	Refs.
	(GHz)	(mas, °)		(mas, °)	($\mu\text{Jy beam}^{-1}$, K)	(mJy beam^{-1} , K)	(mJy)	
(1)	(2)	(3)	(4)	(5)	(6)	(7)	(8)	(9)
HT Lup	239.0	38 × 33, 61	0.5	..., ...	14, 0.24	8.25, 140	77	IV
GW Lup	239.0	45 × 43, 1	0.5	35 × 15, 0	15, 0.17	3.35, 37	89	II
IM Lup	239.0	44 × 43, 115	0.5	33 × 26, 138	14, 0.16	7.11, 80	253	II, III
RU Lup	239.0	25 × 24, 129	-0.5	22 × 10, 6	21, 0.73	3.45, 123	203	II
Sz 114	239.0	67 × 28, 92	0.5	..., ...	19, 0.22	3.36, 38	49	II
Sz 129	239.0	44 × 31, 93	0.0	..., ...	16, 0.25	0.95, 15	86	II
MY Lup	239.0	44 × 43, 122	0.0	39 × 15, 163	16, 0.18	1.78, 20	79	II
HD 142666	231.9	32 × 22, 62	0.5	..., ...	11, 0.35	1.13, 36	120	II
HD 143006	239.0	46 × 45, 51	0.0	42 × 20, 172	15, 0.15	0.67, 7	59	II, IX
AS 205	233.7	38 × 25, 95	0.5	..., ...	16, 0.38	6.15, 145	358	IV
SR 4	239.0	34 × 34, 10	-0.5	35 × 10, 0	25, 0.46	3.40, 63	69	II
Elias 20	239.0	32 × 23, 76	0.0	..., ...	15, 0.44	2.59, 75	104	II
DoAr 25	239.0	48 × 27, 79	0.5	..., ...	13, 0.21	1.84, 30	227	II
Elias 24	231.9	37 × 24, 82	0.0	35 × 10, 166	19, 0.49	4.63, 119	352	II
Elias 27	231.9	49 × 47, 47	0.5	40 × 20, 173	14, 0.14	4.83, 48	330	II, III
DoAr 33	239.0	37 × 24, 75	0.0	20 × 10, 167	17, 0.41	1.89, 46	35	II
WSB 52	239.0	33 × 27, 74	0.0	..., ...	16, 0.38	2.60, 62	67	II, III
WaOph 6	239.0	58 × 54, 84	0.0	55 × 10, 10	17, 0.12	8.67, 59	161	II, III
AS 209	239.0	38 × 36, 68	-0.5	37 × 10, 162	19, 0.30	1.83, 29	288	II, X
HD 163296	239.0	48 × 38, 82	-0.5	..., ...	23, 0.27	4.26, 50	715	II, XI

NOTE—Col. (1) Target name. Col. (2) Mean frequency. Col. (3) Synthesized beam FWHM dimensions and position angle. Col. (4) robust parameter used for visibility weighting. Col. (5) FWHM dimensions and position angle of the adopted taper (if applicable). Col. (6) RMS noise level in the map in both surface brightness and brightness temperature units, measured as described in Section 4.2. Col. (7) The peak intensity in the map, in both surface brightness and brightness temperature units. Col. (8) The integrated flux density inside the adopted `clean` mask. Col. (9) References in the DSHARP article series for additional information: II = Huang et al. (2018a), III = Huang et al. (2018c), IV = Troncoso et al. (2018), IX = Pérez et al. (2018), X = Guzmán et al. (2018), XI = Isella et al. (2018). ← will probably change

methodology for estimating the calibrator fluxes (interpolation in time and frequency from bimonthly monitoring in Bands 3 and 7). About a third of the sample indeed had 5–10% mismatches, but the majority exhibited 15–25% flux scale discrepancies for at least one of the constituent observations. In a few of the more egregious cases, the mismatch was tracked down to a book-keeping issue: the data were pipeline processed before a relevant calibrator catalog update. Some of the others can be attributed to the 2017 November datasets that employed J1427-4206 as the flux calibrator (see Table 2). There is no obvious associated error in the ALMA calibrator catalog, so the issue must be with the interpolation: perhaps this quasar flared or changed its spectrum (or both) between catalog entries. Regardless of the underlying cause, these misalignments were rectified. We selected a reference dataset⁹ and used the `gaintcal` task to re-scale the outlier dataset by a constant that brings it into agreement with the other observations.

⁹ Usually the outlier dataset is obvious because multiple other datasets have good agreement. In one or two examples, a decision on the reference dataset is made based on its quality and proximity in time to measurements in the calibrator catalog.

5. FIDUCIAL DATA PRODUCTS

After the calibration procedure described above was completed, a set of fiducial continuum images were synthesized for further analysis. That imaging largely followed the methodology outlined in Section 4.3, but was tailored to individual sources with the aim of minimizing artifacts in their PSFs. In many cases, this involved adopting a visibility weighting scheme that traded SNR for resolution, as well as a visibility taper to improve the PSF symmetry. Table 4 lists the basic parameters and resulting properties of the fiducial images. The corresponding image gallery is shown in Figure 4. In subsequent DSHARP articles, these are the continuum images used in any analysis unless otherwise stated.

The procedure of synthesizing channel maps of the $^{12}\text{CO } J=2-1$ emission line followed the same basic steps outlined above. The self-calibrated CO visibilities were continuum-subtracted and then imaged in LSRK velocity channels at roughly the native channel spacing (0.35 km s^{-1} ; the actual velocity resolution is about two channels, due to the Hanning smoothing performed in the ALMA correlator). The DSHARP data are generally not sensitive enough to reconstruct useful channel maps of the emission line at the best available resolution. The typical compromise we adopted was to increase the rela-

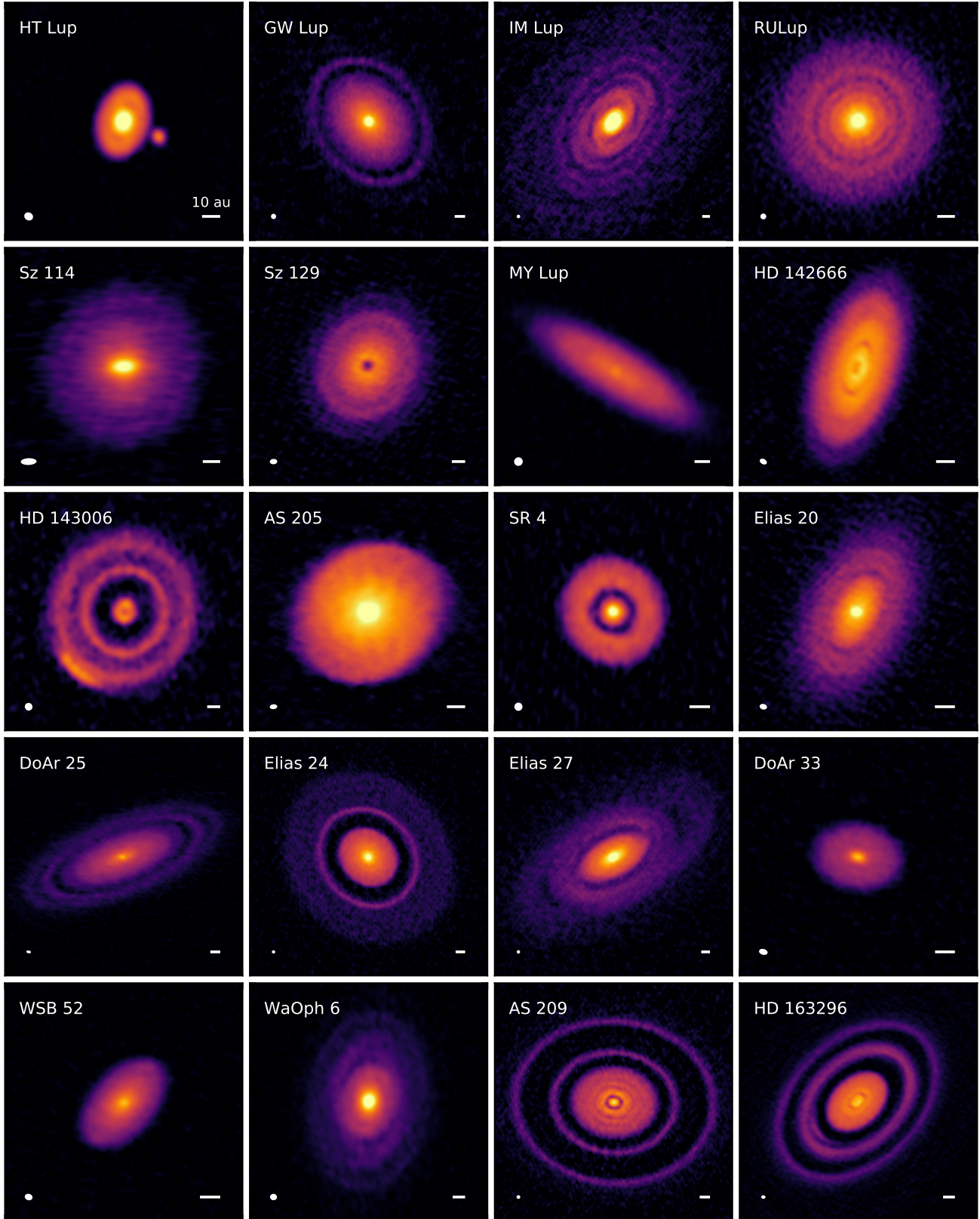


Figure 4. A gallery of 240 GHz (1.25 mm) continuum emission images for the disks in the DSHARP sample. Beam sizes and 10 au scalebars are shown in the lower left and right corners of each panel, respectively. All images are shown on a hyperbolic arcsine stretch to accentuate features over a large intensity dynamic range. There are additional quantitative details available on the image dimensions and intensity scales in the articles by [Huang et al. \(2018a\)](#) and [Troncoso et al. \(2018\)](#).

tive weight on the shorter spatial frequencies (i.e., use a lower `robust` value) and employ a modest taper to provide images with well-behaved PSFs and FWHM resolutions around 100 mas. Table 5 includes the basic parameters of these fiducial channel maps. Figure 5 shows the fiducial channel maps for each individual target.

6. DSHARP DATA RELEASE

One key inspiration for conducting this ALMA Large Program was to provide a set of resources to the community that will help seed and develop a broad range of related work. To that end, we have released a suite of associated DSHARP data products that go beyond the standard contents in the ALMA archive. This release is available online at <http://almascience.nrao.edu/alma-data/DSHARP>. It includes the following:

- the `CASA` scripts and associated `python` modules that were used to process the pipeline-calibrated data (data combination, astrometric and flux calibration corrections, self-calibration, imaging) described in Sections 4.2–4.4;
- fully calibrated continuum and CO $J=2-1$ measurement sets (visibilities used in the initial series of DSHARP articles for analysis and imaging);
- the set of fiducial continuum images (see Table 4 and Figure 4) and CO channel maps (see Table 5 and Figure 5), along with their associated clean masks and PSF images; and
- various secondary data products, including radial intensity profiles, polar image projections (Huang et al. 2018a,c) and the SED data from Figure 1.

With those DSHARP release products and the ALMA archive products (including raw data, pipeline scripts, gain tables, and various quality assurance metrics), the community has the access and resources needed to both reproduce and expand on the efforts detailed in the initial series of DSHARP articles.

7. OVERVIEW OF INITIAL RESULTS

This article has detailed the scientific motivations behind the DSHARP survey, introduced the survey strategy and sample, described the extensive calibration process, and presented the resulting data products as part of a full data release to the community. It is the first in a series of articles in this issue that explore and analyze the DSHARP data in more detail. The key initial conclusions from that work can be summarized as follows:

- Small-scale substructures in protoplanetary disks are ubiquitous. As can be deduced from Figure 4, there is evidence for relative continuum enhancements and/or depletions in all of the disks in the DSHARP sample. These features are found at disk radii from a few au out to more than 100 au.

• The most common form of these substructures are narrow, concentric bright rings/annuli and dark gaps. There are no obvious patterns in their distributions or connections to the stellar host properties. There are hints of additional substructures that are obfuscated due to their smaller size scales (relative to the DSHARP resolution) and/or their modest amplitudes with respect to an optically thick background in the inner disk. Measurements of the rings/annuli and gaps, as well as a more detailed exploration of these associated issues, are presented by Huang et al. (2018a).

- While less common, the spiral morphologies identified for a subset of disks in the DSHARP sample are striking. For the cases with single hosts (IM Lup, WaOph 6, and likely WSB 52), the spiral patterns are complex and appear to be superposed with rings and gaps. Their emission distributions are characterized in detail by Huang et al. (2018c).
- In the two known multiple star systems in the DSHARP sample, HT Lup and AS 205, the disks around the primary stars show clear $m = 2$ spiral modes and complicated CO distributions that are indicative of strong dynamical interactions. The circumstellar material in these systems are presented by Troncoso et al. (2018).
- Prominent azimuthal asymmetries are rare. Substantial deviations from (projected) circular symmetry (or point symmetry for the spiral cases) are only identified in two cases. The disks around HD 143006 and HD 163296 show small, arc-shaped features in otherwise-depleted (i.e., gap) regions. The properties and potential origins of these special cases are scrutinized by Pérez et al. (2018) and Isella et al. (2018), respectively.
- One could make the argument that disk continuum emission can be decomposed into *only* small-scale substructures. The AS 209 disk is a particularly compelling example hinting at that possibility. Guzmán et al. (2018) quantifies its substructures and highlights an important point: there are analogous features lurking in the gas (even as traced by optically thick ^{12}CO), at radii well beyond the extent of the continuum emission.
- The properties of the ring substructures imply that they are the result of particle trapping in gas pressure maxima. Dullemond et al. (2018a) demonstrate that simple models predict similar observables for traps with low turbulence and up to $\sim\text{cm}$ particle sizes, although much larger particles and more moderate turbulence are possible. Hydrodynamics simulations (Zhang et al. 2018)

Table 5. DSHARP Fiducial CO Datacube Properties (still making cubes; no text will change though)

Name	ΔV (km s $^{-1}$)	θ_b , PA $_b$ (mas, °)	robust	θ_{tap} , PA $_{\text{tap}}$ (mas, °)	RMS noise (mJy beam $^{-1}$, K)	peak I_{ν} , T_b (mJy beam $^{-1}$, K)	comments	Refs.
(1)	(2)	(3)	(4)	(5)	(6)	(7)	(8)	(9)
HT Lup								IV
GW Lup								...
IM Lup								III
RU Lup								...
Sz 114								...
Sz 129								...
MY Lup								...
HD 142666								...
HD 143006								IX
AS 205								IV
SR 4								...
Elias 20								...
DoAr 25								...
Elias 24								...
Elias 27								III
DoAr 33								...
WSB 52								III
WaOph 6								III
AS 209	0.35			1.0	...	0.77,		X
HD 163296								XI

NOTE—Col. (1) Target name. Col. (2) Velocity resolution. Col. (3) Synthesized beam FWHM dimensions and position angle. Col. (4) robust parameter used for visibility weighting. Col. (5) FWHM dimensions and position angle of the adopted taper (if applicable). Col. (6) RMS noise level per channel in the maps in both surface brightness and brightness temperature units, measured as described in Section 4.2. Col. (7) The peak intensity in the maps, in both surface brightness and brightness temperature units. Col. (8) The integrated flux density inside the adopted `clean` mask. Col. (9) References in the DSHARP article series for additional information: III = Huang et al. (2018c), IV = Troncoso et al. (2018), IX = Pérez et al. (2018), X = Guzmán et al. (2018), XI = Isella et al. (2018). ← will probably change

and associated models of dust trapping (Dullemond et al. 2018b) suggest that dynamical interactions between low-mass (sub-Jupiter) planets and their local disk material are plausible explanations of the ring-shaped substructure origins.

There is, of course, much more to learn from the DSHARP dataset. Our hope is that this preliminary foray not only provides useful results and motivation for many other studies, but also lays some technical groundwork for designing and calibrating future ALMA surveys of disks at very high angular resolution.

We are grateful to Erica Keller and Tony Remijan for their efforts to pipeline process these data, the ALMA/JAO support staff for pushing through great observations even after the re-configuration delays, Todd Hunter and Crystal Brogan for some useful technical consultations, and Ian Czekala for his advice on measuring stellar host parameters. S. A. and J. H. acknowledge funding support from NASA Exoplanets Research Program grant 80NSSC18K0438. This paper makes use of the following ALMA data: ADS/JAO.ALMA #2016.1.00484.L, ADS/JAO.ALMA #2011.0.00531.S, ADS/JAO.ALMA #2012.1.00694.S, ADS/JAO.ALMA

#2013.1.00226.S, ADS/JAO.ALMA #2013.1.00366.S, ADS/JAO.ALMA #2013.1.00498.S, ADS/JAO.ALMA #2013.1.00631.S, ADS/JAO.ALMA #2013.1.00798.S, ADS/JAO.ALMA #2015.1.00486.S, ADS/JAO.ALMA #2015.1.00964.S. ALMA is a partnership of ESO (representing its member states), NSF (USA) and NINS (Japan), together with NRC (Canada), MOST and ASIAA (Taiwan), and KASI (Republic of Korea), in cooperation with the Republic of Chile. The Joint ALMA Observatory is operated by ESO, AUI/NRAO and NAOJ. This work presents results from the European Space Agency (ESA) space mission *Gaia*. *Gaia* data are being processed by the *Gaia* Data Processing and Analysis Consortium (DPAC). Funding for the DPAC is provided by national institutions, in particular the institutions participating in the *Gaia* Multi-Lateral Agreement (MLA). The *Gaia* mission website is <https://www.cosmos.esa.int/gaia>. The *Gaia* archive website is <https://archives.esac.esa.int/gaia>.

Facilities: ALMA

Software: CASA (McMullin et al. 2007), Numpy (VanDer Walt et al. 2011), Matplotlib (Hunter 2007), Astropy (Astropy Collaboration et al. 2013), ScottiePippen (Czekala et al. 2016, <https://github.com/iancze/ScottiePippen>).

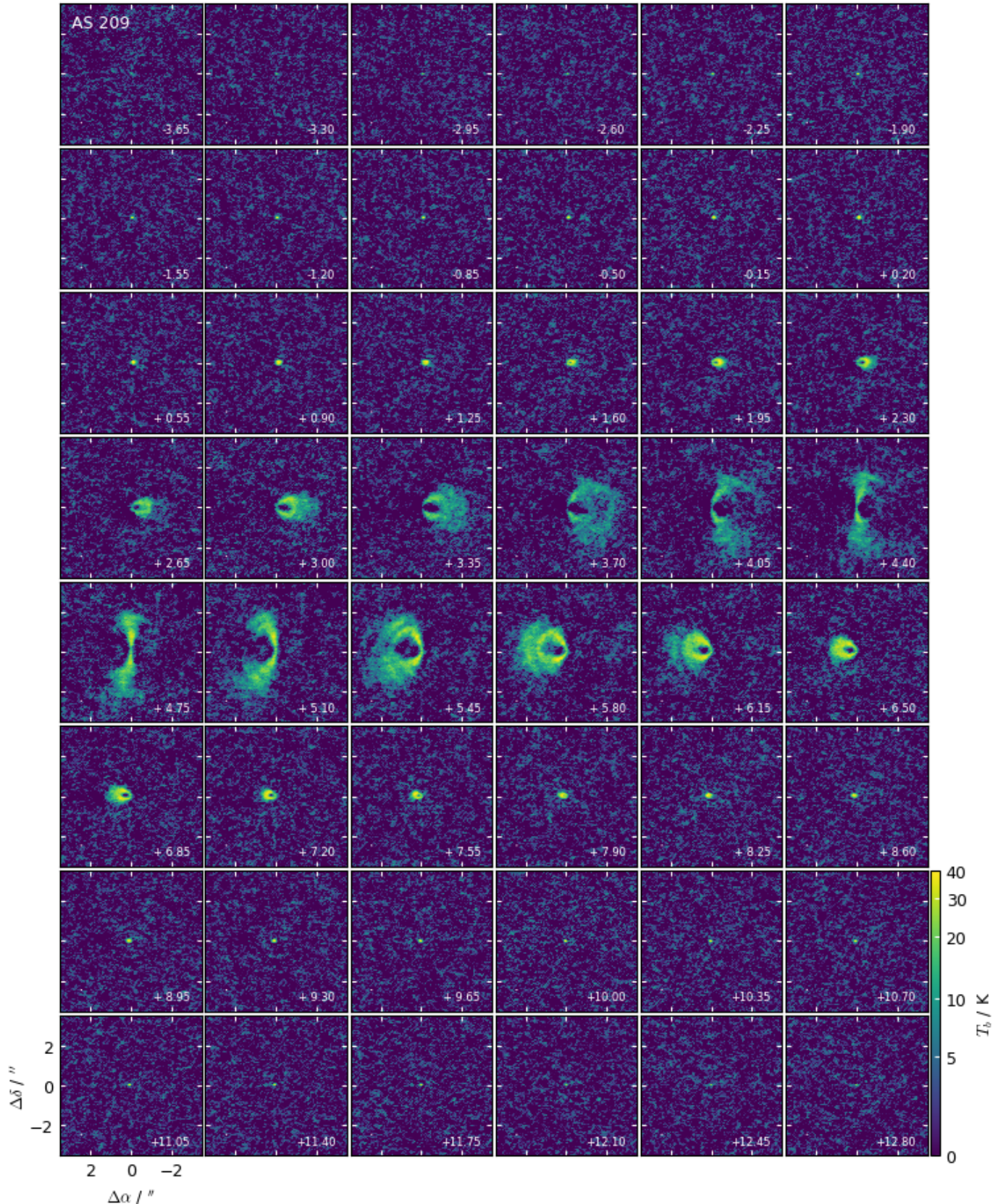


Figure 5a. Channel maps of the ^{12}CO $J=2-1$ line emission from the AS 209 disk. Beam dimensions are shown in the lower left corner of each panel. The LSRK velocity is marked in the lower right corner of each panel.

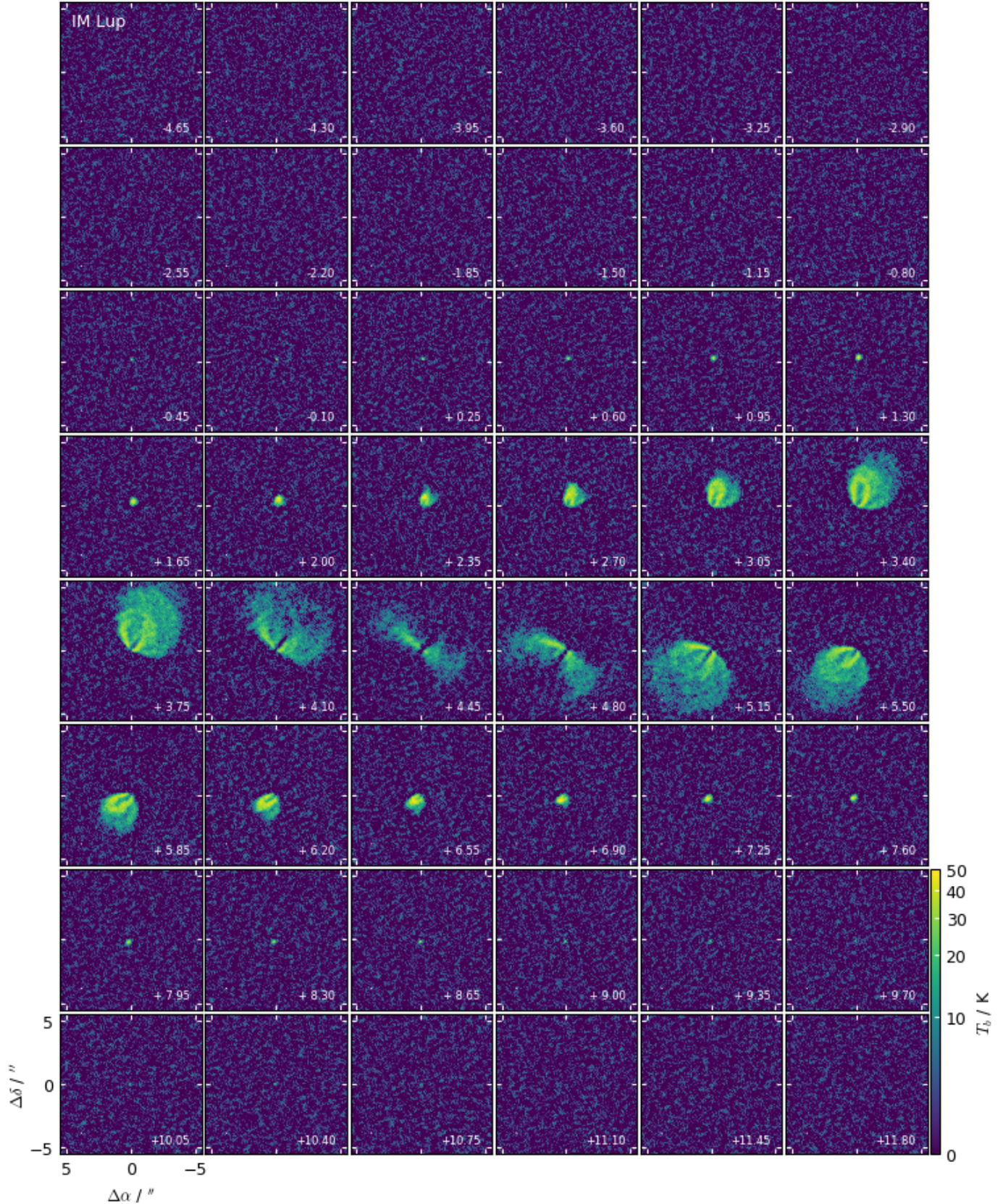


Figure 5b. Channel maps of the ^{12}CO $J=2-1$ line emission from the IM Lup disk. Beam dimensions are shown in the lower left corner of each panel. The LSRK velocity is marked in the lower right corner of each panel.

REFERENCES

- Adachi, I., Hayashi, C., & Nakazawa, K. 1976, *Progress of Theoretical Physics*, 56, 1756, doi: [10.1143/PTP.56.1756](https://doi.org/10.1143/PTP.56.1756)
- Akiyama, E., Hasegawa, Y., Hayashi, M., & Iguchi, S. 2016, *ApJ*, 818, 158, doi: [10.3847/0004-637X/818/2/158](https://doi.org/10.3847/0004-637X/818/2/158)
- Alcalá, J. M., Manara, C. F., Natta, A., et al. 2017, *A&A*, 600, A20, doi: [10.1051/0004-6361/201629929](https://doi.org/10.1051/0004-6361/201629929)
- Alibert, Y., Mordasini, C., Benz, W., & Winisdoerffer, C. 2005, *A&A*, 434, 343, doi: [10.1051/0004-6361:20042032](https://doi.org/10.1051/0004-6361:20042032)
- Allard, F., Guillot, T., Ludwig, H.-G., et al. 2003, in *IAU Symposium*, Vol. 211, Brown Dwarfs, ed. E. Martín, 325
- Allard, F., Homeier, D., & Freytag, B. 2011, in *Astronomical Society of the Pacific Conference Series*, Vol. 448, 16th Cambridge Workshop on Cool Stars, Stellar Systems, and the Sun, ed. C. Johns-Krull, M. K. Browning, & A. A. West, 91
- ALMA Partnership, Brogan, C. L., Pérez, L. M., et al. 2015, *ApJL*, 808, L3, doi: [10.1088/2041-8205/808/1/L3](https://doi.org/10.1088/2041-8205/808/1/L3)
- Andre, P., & Montmerle, T. 1994, *ApJ*, 420, 837, doi: [10.1086/173608](https://doi.org/10.1086/173608)
- Andrews, S. M., Czekala, I., Wilner, D. J., et al. 2010, *ApJ*, 710, 462, doi: [10.1088/0004-637X/710/1/462](https://doi.org/10.1088/0004-637X/710/1/462)
- Andrews, S. M., Rosenfeld, K. A., Kraus, A. L., & Wilner, D. J. 2013, *ApJ*, 771, 129, doi: [10.1088/0004-637X/771/2/129](https://doi.org/10.1088/0004-637X/771/2/129)
- Andrews, S. M., & Williams, J. P. 2005, *ApJ*, 631, 1134, doi: [10.1086/432712](https://doi.org/10.1086/432712)
- . 2007, *ApJ*, 671, 1800, doi: [10.1086/522885](https://doi.org/10.1086/522885)
- Andrews, S. M., Wilner, D. J., Espaillat, C., et al. 2011, *ApJ*, 732, 42, doi: [10.1088/0004-637X/732/1/42](https://doi.org/10.1088/0004-637X/732/1/42)
- Andrews, S. M., Wilner, D. J., Hughes, A. M., Qi, C., & Dullemond, C. P. 2009, *ApJ*, 700, 1502, doi: [10.1088/0004-637X/700/2/1502](https://doi.org/10.1088/0004-637X/700/2/1502)
- Andrews, S. M., Wilner, D. J., Hughes, A. M., et al. 2012, *ApJ*, 744, 162, doi: [10.1088/0004-637X/744/2/162](https://doi.org/10.1088/0004-637X/744/2/162)
- Andrews, S. M., Wilner, D. J., Zhu, Z., et al. 2016, *ApJL*, 820, L40, doi: [10.3847/2041-8205/820/2/L40](https://doi.org/10.3847/2041-8205/820/2/L40)
- . 2018, *ApJL*, 820, L40, doi: [10.3847/2041-8205/820/2/L40](https://doi.org/10.3847/2041-8205/820/2/L40)
- Ansdell, M., Williams, J. P., van der Marel, N., et al. 2016, *ApJ*, 828, 46, doi: [10.3847/0004-637X/828/1/46](https://doi.org/10.3847/0004-637X/828/1/46)
- Ansdell, M., Williams, J. P., Trapman, L., et al. 2018, *ApJ*, 859, 21, doi: [10.3847/1538-4357/aab890](https://doi.org/10.3847/1538-4357/aab890)
- Armitage, P. J., Eisner, J. A., & Simon, J. B. 2016, *ApJL*, 828, L2, doi: [10.3847/2041-8205/828/1/L2](https://doi.org/10.3847/2041-8205/828/1/L2)
- Astraatmadja, T. L., & Bailer-Jones, C. A. L. 2016, *ApJ*, 832, 137, doi: [10.3847/0004-637X/832/2/137](https://doi.org/10.3847/0004-637X/832/2/137)
- Astropy Collaboration, Robitaille, T. P., Tollerud, E. J., et al. 2013, *A&A*, 558, A33, doi: [10.1051/0004-6361/201322068](https://doi.org/10.1051/0004-6361/201322068)
- Avenhaus, H., Quanz, S. P., Schmid, H. M., et al. 2014, *ApJ*, 781, 87, doi: [10.1088/0004-637X/781/2/87](https://doi.org/10.1088/0004-637X/781/2/87)
- Avenhaus, H., Quanz, S. P., Garufi, A., et al. 2018, *ArXiv e-prints*. <https://arxiv.org/abs/1803.10882>
- Bai, X.-N. 2014, *ApJ*, 791, 137, doi: [10.1088/0004-637X/791/2/137](https://doi.org/10.1088/0004-637X/791/2/137)
- Barenfeld, S. A., Carpenter, J. M., Ricci, L., & Isella, A. 2016, *ApJ*, 827, 142, doi: [10.3847/0004-637X/827/2/142](https://doi.org/10.3847/0004-637X/827/2/142)
- . 2017, *ApJ*, 827, 142, doi: [10.3847/0004-637X/827/2/142](https://doi.org/10.3847/0004-637X/827/2/142)
- Barge, P., & Sommeria, J. 1995, *A&A*, 295, L1
- Benisty, M., Juhasz, A., Boccaletti, A., et al. 2015, *A&A*, 578, L6, doi: [10.1051/0004-6361/201526011](https://doi.org/10.1051/0004-6361/201526011)
- Benz, W., Ida, S., Alibert, Y., Lin, D., & Mordasini, C. 2014, *Protostars and Planets VI*, 691, doi: [10.2458/azu_uapress_9780816531240-ch030](https://doi.org/10.2458/azu_uapress_9780816531240-ch030)
- Birnstiel, T., & Andrews, S. M. 2014, *ApJ*, 780, 153, doi: [10.1088/0004-637X/780/2/153](https://doi.org/10.1088/0004-637X/780/2/153)
- Birnstiel, T., Fang, M., & Johansen, A. 2016, *SSRv*, 205, 41, doi: [10.1007/s11214-016-0256-1](https://doi.org/10.1007/s11214-016-0256-1)
- Bouvier, J., & Appenzeller, I. 1992, *A&AS*, 92, 481
- Brauer, F., Dullemond, C. P., & Henning, T. 2008, *A&A*, 480, 859, doi: [10.1051/0004-6361:20077759](https://doi.org/10.1051/0004-6361:20077759)
- Brauer, F., Dullemond, C. P., Johansen, A., et al. 2007, *A&A*, 469, 1169, doi: [10.1051/0004-6361:20066865](https://doi.org/10.1051/0004-6361:20066865)
- Calvet, N., D'Alessio, P., Hartmann, L., et al. 2002, *ApJ*, 568, 1008, doi: [10.1086/339061](https://doi.org/10.1086/339061)
- Cambrésy, L. 1999, *A&A*, 345, 965
- Carpenter, J. M., Bouwman, J., Silverstone, M. D., et al. 2008, *The Astrophysical Journal Supplement Series*, 179, 423, doi: [10.1086/592274](https://doi.org/10.1086/592274)
- Casassus, S., van der Plas, G., M, S. P., et al. 2013, *Nature*, 493, 191, doi: [10.1038/nature11769](https://doi.org/10.1038/nature11769)
- Casassus, S., Avenhaus, H., Pérez, S., et al. 2018, *MNRAS*, 477, 5104, doi: [10.1093/mnras/sty894](https://doi.org/10.1093/mnras/sty894)
- Choi, J., Dotter, A., Conroy, C., et al. 2016, *ApJ*, 823, 102, doi: [10.3847/0004-637X/823/2/102](https://doi.org/10.3847/0004-637X/823/2/102)
- Christiaens, V., Casassus, S., Perez, S., van der Plas, G., & Ménard, F. 2014, *ApJL*, 785, L12, doi: [10.1088/2041-8205/785/1/L12](https://doi.org/10.1088/2041-8205/785/1/L12)
- Cieza, L. A., Casassus, S., Tobin, J., et al. 2016, *Nature*, 535, 258, doi: [10.1038/nature18612](https://doi.org/10.1038/nature18612)
- Cieza, L. A., Casassus, S., Pérez, S., et al. 2017, *ApJL*, 851, L23, doi: [10.3847/2041-8213/aa9b7b](https://doi.org/10.3847/2041-8213/aa9b7b)
- Cleeves, L. I., Öberg, K. I., Wilner, D. J., et al. 2016, *ApJ*, 832, 110, doi: [10.3847/0004-637X/832/2/110](https://doi.org/10.3847/0004-637X/832/2/110)
- Comerón, F. 2008, *The Lupus Clouds*, ed. B. Reipurth, 295
- Cornwell, T. J. 2008, *IEEE Journal of Selected Topics in Signal Processing*, 2, 793, doi: [10.1109/JSTSP.2008.2006388](https://doi.org/10.1109/JSTSP.2008.2006388)

- Cox, E. G., Harris, R. J., Looney, L. W., et al. 2017, *ApJ*, 851, 83, doi: [10.3847/1538-4357/aa97e2](https://doi.org/10.3847/1538-4357/aa97e2)
- Czekala, I., Andrews, S. M., Torres, G., et al. 2016, *ApJ*, 818, 156, doi: [10.3847/0004-637X/818/2/156](https://doi.org/10.3847/0004-637X/818/2/156)
- de Boer, J., Salter, G., Benisty, M., et al. 2016, *A&A*, 595, A114, doi: [10.1051/0004-6361/201629267](https://doi.org/10.1051/0004-6361/201629267)
- de Geus, E. J., de Zeeuw, P. T., & Lub, J. 1989, *A&A*, 216, 44
- de Gregorio-Monsalvo, I., Ménard, F., Dent, W., et al. 2013, *A&A*, 557, A133, doi: [10.1051/0004-6361/201321603](https://doi.org/10.1051/0004-6361/201321603)
- Dent, W. R. F., Matthews, H. E., & Ward-Thompson, D. 1998, *MNRAS*, 301, 1049, doi: [10.1046/j.1365-8711.1998.02091.x](https://doi.org/10.1046/j.1365-8711.1998.02091.x)
- Dipierro, G., Pinilla, P., Lodato, G., & Testi, L. 2015, ArXiv e-prints. <https://arxiv.org/abs/1504.08099>
- Dipierro, G., Ricci, L., Pérez, L., et al. 2018, *MNRAS*, 475, 5296, doi: [10.1093/mnras/sty181](https://doi.org/10.1093/mnras/sty181)
- Dong, R., Liu, S.-y., Eisner, J., et al. 2018, *ApJ*, 860, 124, doi: [10.3847/1538-4357/aac6cb](https://doi.org/10.3847/1538-4357/aac6cb)
- Dullemond, C. P., & Penzlin, A. B. T. 2018, *A&A*, 609, A50, doi: [10.1051/0004-6361/201731878](https://doi.org/10.1051/0004-6361/201731878)
- Dullemond, C. P., Birnstiel, T., Andrews, S. M., et al. 2018a, *ApJL*
- . 2018b, *ApJL*
- Dzyurkevich, N., Turner, N. J., Henning, T., & Kley, W. 2013, *ApJ*, 765, 114, doi: [10.1088/0004-637X/765/2/114](https://doi.org/10.1088/0004-637X/765/2/114)
- Eisner, J. A., Hillenbrand, L. A., White, R. J., Akeson, R. L., & Sargent, A. I. 2005, *ApJ*, 623, 952, doi: [10.1086/428828](https://doi.org/10.1086/428828)
- Evans, II, N. J., Dunham, M. M., Jørgensen, J. K., et al. 2009, *ApJS*, 181, 321, doi: [10.1088/0067-0049/181/2/321](https://doi.org/10.1088/0067-0049/181/2/321)
- Facchini, S., Birnstiel, T., Bruderer, S., & van Dishoeck, E. F. 2017, *A&A*, 605, A16, doi: [10.1051/0004-6361/201630329](https://doi.org/10.1051/0004-6361/201630329)
- Fairlamb, J. R., Oudmaijer, R. D., Mendigutía, I., Ille, J. D., & van den Ancker, M. E. 2015, *MNRAS*, 453, 976, doi: [10.1093/mnras/stv1576](https://doi.org/10.1093/mnras/stv1576)
- Fedele, D., Carney, M., Hogerheijde, M. R., et al. 2017, *A&A*, 600, A72, doi: [10.1051/0004-6361/201629860](https://doi.org/10.1051/0004-6361/201629860)
- Fedele, D., Tazzari, M., Booth, R., et al. 2018, *A&A*, 610, A24, doi: [10.1051/0004-6361/201731978](https://doi.org/10.1051/0004-6361/201731978)
- Flaherty, K. M., Hughes, A. M., Rosenfeld, K. A., et al. 2015, *ApJ*, 813, 99, doi: [10.1088/0004-637X/813/2/99](https://doi.org/10.1088/0004-637X/813/2/99)
- Flaherty, K. M., Hughes, A. M., Rose, S. C., et al. 2017, *ApJ*, 843, 150, doi: [10.3847/1538-4357/aa79f9](https://doi.org/10.3847/1538-4357/aa79f9)
- Flock, M., Ruge, J. P., Dzyurkevich, N., et al. 2015, *A&A*, 574, A68, doi: [10.1051/0004-6361/201424693](https://doi.org/10.1051/0004-6361/201424693)
- Fung, J., Shi, J.-M., & Chiang, E. 2014, *ApJ*, 782, 88, doi: [10.1088/0004-637X/782/2/88](https://doi.org/10.1088/0004-637X/782/2/88)
- Gaia Collaboration, Brown, A. G. A., Vallenari, A., et al. 2018, ArXiv e-prints. <https://arxiv.org/abs/1804.09365>
- Ghez, A. M., McCarthy, D. W., Patience, J. L., & Beck, T. L. 1997, *ApJ*, 481, 378, doi: [10.1086/304031](https://doi.org/10.1086/304031)
- Ghez, A. M., Neugebauer, G., & Matthews, K. 1993, *AJ*, 106, 2005, doi: [10.1086/116782](https://doi.org/10.1086/116782)
- Ginski, C., Stolker, T., Pinilla, P., et al. 2016, *A&A*, 595, A112, doi: [10.1051/0004-6361/201629265](https://doi.org/10.1051/0004-6361/201629265)
- Goodman, J., Narayan, R., & Goldreich, P. 1987, *MNRAS*, 225, 695, doi: [10.1093/mnras/225.3.695](https://doi.org/10.1093/mnras/225.3.695)
- Grady, C. A., Muto, T., Hashimoto, J., et al. 2013, *ApJ*, 762, 48, doi: [10.1088/0004-637X/762/1/48](https://doi.org/10.1088/0004-637X/762/1/48)
- Grankin, K. N., Melnikov, S. Y., Bouvier, J., Herbst, W., & Shevchenko, V. S. 2007, *A&A*, 461, 183, doi: [10.1051/0004-6361:20065489](https://doi.org/10.1051/0004-6361:20065489)
- Gras-Velázquez, Á., & Ray, T. P. 2005, *A&A*, 443, 541, doi: [10.1051/0004-6361:20042397](https://doi.org/10.1051/0004-6361:20042397)
- Greaves, J. S., & Rice, W. K. M. 2010, *MNRAS*, 407, 1981, doi: [10.1111/j.1365-2966.2010.17043.x](https://doi.org/10.1111/j.1365-2966.2010.17043.x)
- Guilloteau, S., Dutrey, A., Piétu, V., & Boehler, Y. 2011, *A&A*, 529, A105, doi: [10.1051/0004-6361/201015209](https://doi.org/10.1051/0004-6361/201015209)
- Guzmán, V. V., Andrews, S. M., Bai, X., et al. 2018, *ApJL*
- Henning, T., Burkert, A., Launhardt, R., Leinert, C., & Stecklum, B. 1998, *A&A*, 336, 565
- Herbig, G. H., & Bell, K. R. 1988, *Third Catalog of Emission-Line Stars of the Orion Population : 3 : 1988*
- Herbst, W., Herbst, D. K., Grossman, E. J., & Weinstein, D. 1994, *AJ*, 108, 1906, doi: [10.1086/117204](https://doi.org/10.1086/117204)
- Huang, J., Öberg, K. I., Qi, C., et al. 2017, *ApJ*, 835, 231, doi: [10.3847/1538-4357/835/2/231](https://doi.org/10.3847/1538-4357/835/2/231)
- Huang, J., Andrews, S. M., Bai, X., et al. 2018a, *ApJL*
- Huang, J., Andrews, S. M., Cleeves, L. I., et al. 2018b, *ApJ*, 852, 122, doi: [10.3847/1538-4357/aaa1e7](https://doi.org/10.3847/1538-4357/aaa1e7)
- Huang, J., Andrews, S. M., Bai, X., et al. 2018c, *ApJL*
- Hughes, J., Hartigan, P., Krautter, J., & Kelemen, J. 1994, *AJ*, 108, 1071, doi: [10.1086/117135](https://doi.org/10.1086/117135)
- Hunter, J. D. 2007, *Computing In Science & Engineering*, 9, 90
- Ida, S., & Lin, D. N. C. 2004, *ApJ*, 604, 388, doi: [10.1086/381724](https://doi.org/10.1086/381724)
- . 2008, *ApJ*, 673, 487, doi: [10.1086/523754](https://doi.org/10.1086/523754)
- Isella, A., Carpenter, J. M., & Sargent, A. I. 2009, *ApJ*, 701, 260, doi: [10.1088/0004-637X/701/1/260](https://doi.org/10.1088/0004-637X/701/1/260)
- . 2010, *ApJ*, 714, 1746, doi: [10.1088/0004-637X/714/2/1746](https://doi.org/10.1088/0004-637X/714/2/1746)
- Isella, A., Pérez, L. M., Carpenter, J. M., et al. 2013, *ApJ*, 775, 30, doi: [10.1088/0004-637X/775/1/30](https://doi.org/10.1088/0004-637X/775/1/30)
- Isella, A., Testi, L., Natta, A., et al. 2007, *A&A*, 469, 213, doi: [10.1051/0004-6361:20077385](https://doi.org/10.1051/0004-6361:20077385)

- Isella, A., Guidi, G., Testi, L., et al. 2016, *PhRvL*, 117, 251101
- Isella, A., Andrews, S. M., Bai, X., et al. 2018, *ApJL*
- Ishihara, D., Onaka, T., Kataza, H., et al. 2010, *A&A*, 514, A1, doi: [10.1051/0004-6361/200913811](https://doi.org/10.1051/0004-6361/200913811)
- Johansen, A., Blum, J., Tanaka, H., et al. 2014, in *Protostars & Planets VI*, eds. H. Beuther, R. Klessen, C. Dullemond, & Th. Henning (Univ. Arizona Press: Tucson), in press. <https://arxiv.org/abs/1402.1344>
- Johansen, A., Youdin, A., & Klahr, H. 2009, *ApJ*, 697, 1269, doi: [10.1088/0004-637X/697/2/1269](https://doi.org/10.1088/0004-637X/697/2/1269)
- Lin, D. N. C., & Papaloizou, J. C. B. 1993, in *Protostars and Planets III*, ed. E. H. Levy & J. I. Lunine, 749–835
- Loinard, L., Torres, R. M., Mioduszewski, A. J., & Rodríguez, L. F. 2008, *ApJL*, 675, L29, doi: [10.1086/529548](https://doi.org/10.1086/529548)
- Lommen, D., Maddison, S. T., Wright, C. M., et al. 2009, *A&A*, 495, 869, doi: [10.1051/0004-6361:200810999](https://doi.org/10.1051/0004-6361:200810999)
- Lommen, D., Wright, C. M., Maddison, S. T., et al. 2007, *A&A*, 462, 211, doi: [10.1051/0004-6361:20066255](https://doi.org/10.1051/0004-6361:20066255)
- Loomis, R. A., Öberg, K. I., Andrews, S. M., & MacGregor, M. A. 2017, *ApJ*, 840, 23, doi: [10.3847/1538-4357/aa6c63](https://doi.org/10.3847/1538-4357/aa6c63)
- Luhman, K. L., Herrmann, K. A., Mamajek, E. E., Esplin, T. L., & Pecaut, M. J. 2018, ArXiv e-prints. <https://arxiv.org/abs/1807.07955>
- Luhman, K. L., & Mamajek, E. E. 2012, *ApJ*, 758, 31, doi: [10.1088/0004-637X/758/1/31](https://doi.org/10.1088/0004-637X/758/1/31)
- Luhman, K. L., & Rieke, G. H. 1999, *ApJ*, 525, 440, doi: [10.1086/307891](https://doi.org/10.1086/307891)
- Lyra, W., Turner, N. J., & McNally, C. P. 2015, *A&A*, 574, A10, doi: [10.1051/0004-6361/201424919](https://doi.org/10.1051/0004-6361/201424919)
- Manara, C. F., Rosotti, G., Testi, L., et al. 2016, *A&A*, 591, L3, doi: [10.1051/0004-6361/201628549](https://doi.org/10.1051/0004-6361/201628549)
- Mannings, V., & Emerson, J. P. 1994, *MNRAS*, 267, 361
- Mannings, V., & Sargent, A. I. 1997, *ApJ*, 490, 792, doi: [10.1086/304897](https://doi.org/10.1086/304897)
- Marino, S., Perez, S., & Casassus, S. 2015, *ApJL*, 798, L44, doi: [10.1088/2041-8205/798/2/L44](https://doi.org/10.1088/2041-8205/798/2/L44)
- McMullin, J. P., Waters, B., Schiebel, D., Young, W., & Golap, K. 2007, in *Astronomical Society of the Pacific Conference Series*, Vol. 376, *Astronomical Data Analysis Software and Systems XVI*, ed. R. A. Shaw, F. Hill, & D. J. Bell, 127
- Mendigutía, I., Mora, A., Montesinos, B., et al. 2012, *A&A*, 543, A59, doi: [10.1051/0004-6361/201219110](https://doi.org/10.1051/0004-6361/201219110)
- Menu, J., van Boekel, R., Henning, T., et al. 2014, *A&A*, 564, A93, doi: [10.1051/0004-6361/201322961](https://doi.org/10.1051/0004-6361/201322961)
- Merín, B., Jørgensen, J., Spezzi, L., et al. 2008, *ApJS*, 177, 551, doi: [10.1086/588042](https://doi.org/10.1086/588042)
- Mohanty, S., Greaves, J., Mortlock, D., et al. 2013, *ApJ*, 773, 168, doi: [10.1088/0004-637X/773/2/168](https://doi.org/10.1088/0004-637X/773/2/168)
- Mordasini, C., Alibert, Y., & Benz, W. 2009, *A&A*, 501, 1139, doi: [10.1051/0004-6361/200810301](https://doi.org/10.1051/0004-6361/200810301)
- Mulders, G. D., Pascucci, I., Manara, C. F., et al. 2017, *ApJ*, 847, 31, doi: [10.3847/1538-4357/aa8906](https://doi.org/10.3847/1538-4357/aa8906)
- Muto, T., Grady, C. A., Hashimoto, J., et al. 2012, *ApJL*, 748, L22, doi: [10.1088/2041-8205/748/2/L22](https://doi.org/10.1088/2041-8205/748/2/L22)
- Muzerolle, J., Hartmann, L., & Calvet, N. 1998, *AJ*, 116, 2965, doi: [10.1086/300636](https://doi.org/10.1086/300636)
- Najita, J. R., & Kenyon, S. J. 2014, *MNRAS*, 445, 3315, doi: [10.1093/mnras/stu1994](https://doi.org/10.1093/mnras/stu1994)
- Nakagawa, Y., Sekiya, M., & Hayashi, C. 1986, *Icarus*, 67, 375, doi: [10.1016/0019-1035\(86\)90121-1](https://doi.org/10.1016/0019-1035(86)90121-1)
- Natta, A., Testi, L., Neri, R., Shepherd, D. S., & Wilner, D. J. 2004, *A&A*, 416, 179, doi: [10.1051/0004-6361:20035620](https://doi.org/10.1051/0004-6361:20035620)
- Natta, A., Testi, L., & Randich, S. 2006, *A&A*, 452, 245, doi: [10.1051/0004-6361:20054706](https://doi.org/10.1051/0004-6361:20054706)
- Nixon, C. J., King, A. R., & Pringle, J. E. 2018, *MNRAS*, 477, 3273, doi: [10.1093/mnras/sty593](https://doi.org/10.1093/mnras/sty593)
- Nuernberger, D., Chini, R., & Zinnecker, H. 1997, *A&A*, 324, 1036
- Öberg, K. I., Qi, C., Fogel, J. K. J., et al. 2011, *ApJ*, 734, 98, doi: [10.1088/0004-637X/734/2/98](https://doi.org/10.1088/0004-637X/734/2/98)
- Okuzumi, S., Tanaka, H., Kobayashi, H., & Wada, K. 2012, *ApJ*, 752, 106, doi: [10.1088/0004-637X/752/2/106](https://doi.org/10.1088/0004-637X/752/2/106)
- Oudmaijer, R. D., Palacios, J., Eiroa, C., et al. 2001, *A&A*, 379, 564, doi: [10.1051/0004-6361:20011331](https://doi.org/10.1051/0004-6361:20011331)
- Paardekooper, S.-J., & Mellema, G. 2006, *A&A*, 453, 1129, doi: [10.1051/0004-6361:20054449](https://doi.org/10.1051/0004-6361:20054449)
- Padgett, D. L., Cieza, L., Stapelfeldt, K. R., et al. 2006, *ApJ*, 645, 1283, doi: [10.1086/504374](https://doi.org/10.1086/504374)
- Panić, O., Hogerheijde, M. R., Wilner, D., & Qi, C. 2009, *A&A*, 501, 269, doi: [10.1051/0004-6361/200911883](https://doi.org/10.1051/0004-6361/200911883)
- Pascucci, I., Testi, L., Herczeg, G. J., et al. 2016, *ApJ*, 831, 125, doi: [10.3847/0004-637X/831/2/125](https://doi.org/10.3847/0004-637X/831/2/125)
- Pérez, L., Andrews, S. M., Bai, X., et al. 2018, *ApJL*
- Pérez, L. M., Isella, A., Carpenter, J. M., & Chandler, C. J. 2014, *ApJL*, 783, L13, doi: [10.1088/2041-8205/783/1/L13](https://doi.org/10.1088/2041-8205/783/1/L13)
- . 2015, *ApJL*, 783, L13, doi: [10.1088/2041-8205/783/1/L13](https://doi.org/10.1088/2041-8205/783/1/L13)
- Pérez, L. M., Carpenter, J. M., Chandler, C. J., et al. 2012, *ApJL*, 760, L17, doi: [10.1088/2041-8205/760/1/L17](https://doi.org/10.1088/2041-8205/760/1/L17)
- Pérez, L. M., Carpenter, J. M., Andrews, S. M., et al. 2016, *Science*, 353, 1519, doi: [10.1126/science.aaf8296](https://doi.org/10.1126/science.aaf8296)
- Pinilla, P., Benisty, M., & Birnstiel, T. 2012, *A&A*, 545, A81, doi: [10.1051/0004-6361/201219315](https://doi.org/10.1051/0004-6361/201219315)
- Pinilla, P., Pohl, A., Stammler, S. M., & Birnstiel, T. 2017, *ApJ*, 845, 68, doi: [10.3847/1538-4357/aa7edb](https://doi.org/10.3847/1538-4357/aa7edb)

- Pinilla, P., Tazzari, M., Pascucci, I., et al. 2018, *ApJ*, 859, 32, doi: [10.3847/1538-4357/aabf94](https://doi.org/10.3847/1538-4357/aabf94)
- Pinte, C., Padgett, D. L., Ménard, F., et al. 2008, *A&A*, 489, 633, doi: [10.1051/0004-6361:200810121](https://doi.org/10.1051/0004-6361:200810121)
- Pinte, C., Ménard, F., Duchêne, G., et al. 2018, *A&A*, 609, A47, doi: [10.1051/0004-6361/201731377](https://doi.org/10.1051/0004-6361/201731377)
- Preibisch, T., & Mamajek, E. 2008, The Nearest OB Association: Scorpius-Centaurus (Sco OB2), ed. B. Reipurth, 235
- Qi, C., Öberg, K. I., Andrews, S. M., et al. 2015, *ApJ*, 813, 128, doi: [10.1088/0004-637X/813/2/128](https://doi.org/10.1088/0004-637X/813/2/128)
- Quanz, S. P., Avenhaus, H., Buenzli, E., et al. 2013, *ApJL*, 766, L2, doi: [10.1088/2041-8205/766/1/L2](https://doi.org/10.1088/2041-8205/766/1/L2)
- Ribas, Á., Espaillat, C. C., Macías, E., et al. 2017, *ApJ*, 849, 63, doi: [10.3847/1538-4357/aa8e99](https://doi.org/10.3847/1538-4357/aa8e99)
- Ricci, L., Testi, L., Natta, A., & Brooks, K. J. 2010, *A&A*, 521, A66, doi: [10.1051/0004-6361/201015039](https://doi.org/10.1051/0004-6361/201015039)
- Rice, W. K. M., Armitage, P. J., Wood, K., & Lodato, G. 2006, *MNRAS*, 373, 1619, doi: [10.1111/j.1365-2966.2006.11113.x](https://doi.org/10.1111/j.1365-2966.2006.11113.x)
- Rigliaco, E., Pascucci, I., Duchene, G., et al. 2015, *ApJ*, 801, 31, doi: [10.1088/0004-637X/801/1/31](https://doi.org/10.1088/0004-637X/801/1/31)
- Roccatagliata, V., Henning, T., Wolf, S., et al. 2009, *A&A*, 497, 409, doi: [10.1051/0004-6361/200811018](https://doi.org/10.1051/0004-6361/200811018)
- Rosenfeld, K. A., Andrews, S. M., Wilner, D. J., Kastner, J. H., & McClure, M. K. 2013, *ApJ*, 775, 136, doi: [10.1088/0004-637X/775/2/136](https://doi.org/10.1088/0004-637X/775/2/136)
- Rosenfeld, K. A., Chiang, E., & Andrews, S. M. 2014, *ApJ*, 782, 62, doi: [10.1088/0004-637X/782/2/62](https://doi.org/10.1088/0004-637X/782/2/62)
- Rosenfeld, K. A., Qi, C., Andrews, S. M., et al. 2012, *ApJ*, 757, 129, doi: [10.1088/0004-637X/757/2/129](https://doi.org/10.1088/0004-637X/757/2/129)
- Salyk, C., Herczeg, G. J., Brown, J. M., et al. 2013, *ApJ*, 769, 21, doi: [10.1088/0004-637X/769/1/21](https://doi.org/10.1088/0004-637X/769/1/21)
- Salyk, C., Pontoppidan, K., Corder, S., et al. 2014, *ApJ*, 792, 68, doi: [10.1088/0004-637X/792/1/68](https://doi.org/10.1088/0004-637X/792/1/68)
- Sandell, G., Weintraub, D. A., & Hamidouche, M. 2011, *ApJ*, 727, 26, doi: [10.1088/0004-637X/727/1/26](https://doi.org/10.1088/0004-637X/727/1/26)
- Simon, J. B., & Armitage, P. J. 2014, *ApJ*, 784, 15, doi: [10.1088/0004-637X/784/1/15](https://doi.org/10.1088/0004-637X/784/1/15)
- Skrutskie, M. F., Dutkiewitch, D., Strom, S. E., et al. 1990, *AJ*, 99, 1187, doi: [10.1086/115407](https://doi.org/10.1086/115407)
- Skrutskie, M. F., Cutri, R. M., Stiening, R., et al. 2006, *AJ*, 131, 1163, doi: [10.1086/498708](https://doi.org/10.1086/498708)
- Soderblom, D. R., Hillenbrand, L. A., Jeffries, R. D., Mamajek, E. E., & Naylor, T. 2014, Protostars and Planets VI, 219, doi: [10.2458/azu_uapress_9780816531240-ch010](https://doi.org/10.2458/azu_uapress_9780816531240-ch010)
- Stammler, S. M., Birnstiel, T., Panić, O., Dullemond, C. P., & Dominik, C. 2017, *A&A*, 600, A140, doi: [10.1051/0004-6361/201629041](https://doi.org/10.1051/0004-6361/201629041)
- Stanke, T., Smith, M. D., Gredel, R., & Khanzadyan, T. 2006, *A&A*, 447, 609, doi: [10.1051/0004-6361:20041331](https://doi.org/10.1051/0004-6361:20041331)
- Strom, K. M., Strom, S. E., Edwards, S., Cabrit, S., & Skrutskie, M. F. 1989, *AJ*, 97, 1451, doi: [10.1086/115085](https://doi.org/10.1086/115085)
- Sylvester, R. J., Skinner, C. J., Barlow, M. J., & Mannings, V. 1996, *MNRAS*, 279, 915, doi: [10.1093/mnras/279.3.915](https://doi.org/10.1093/mnras/279.3.915)
- Takeuchi, T., & Lin, D. N. C. 2002, *ApJ*, 581, 1344, doi: [10.1086/344437](https://doi.org/10.1086/344437)
- . 2005, *ApJ*, 623, 482, doi: [10.1086/428378](https://doi.org/10.1086/428378)
- Tazzari, M., Testi, L., Ercolano, B., et al. 2016, *A&A*, 588, A53, doi: [10.1051/0004-6361/201527423](https://doi.org/10.1051/0004-6361/201527423)
- Tazzari, M., Testi, L., Natta, A., et al. 2017, ArXiv e-prints. <https://arxiv.org/abs/1707.01499>
- Testi, L., Birnstiel, T., Ricci, L., et al. 2014, Protostars and Planets VI, 339, doi: [10.2458/azu_uapress_9780816531240-ch015](https://doi.org/10.2458/azu_uapress_9780816531240-ch015)
- Tripathi, A., Andrews, S. M., Birnstiel, T., & Wilner, D. J. 2017, *ApJ*, 845, 44, doi: [10.3847/1538-4357/aa7c62](https://doi.org/10.3847/1538-4357/aa7c62)
- Tripathi, A., Andrews, S. M., Birnstiel, T., et al. 2018, ArXiv e-prints. <https://arxiv.org/abs/1805.06457>
- Troncoso, N., Pérez, L. M., Andrews, S. M., et al. 2018, *ApJL*
- Ubach, C., Maddison, S. T., Wright, C. M., et al. 2017, *MNRAS*, 466, 4083, doi: [10.1093/mnras/stx012](https://doi.org/10.1093/mnras/stx012)
- van der Marel, N., Cazzoletti, P., Pinilla, P., & Garufi, A. 2016, *ApJ*, 832, 178, doi: [10.3847/0004-637X/832/2/178](https://doi.org/10.3847/0004-637X/832/2/178)
- van der Marel, N., van Dishoeck, E. F., Bruderer, S., et al. 2013, *Science*, 340, 1199, doi: [10.1126/science.1236770](https://doi.org/10.1126/science.1236770)
- van der Marel, N., Williams, J. P., Ansdell, M., et al. 2018, *ApJ*, 854, 177, doi: [10.3847/1538-4357/aaa46b](https://doi.org/10.3847/1538-4357/aaa46b)
- van der Plas, G., Wright, C. M., Ménard, F., et al. 2017, *A&A*, 597, A32, doi: [10.1051/0004-6361/201629523](https://doi.org/10.1051/0004-6361/201629523)
- Van Der Walt, S., Colbert, S. C., & Varoquaux, G. 2011, ArXiv e-prints. <https://arxiv.org/abs/1102.1523>
- van Terwisga, S. E., van Dishoeck, E. F., Ansdell, M., et al. 2018, ArXiv e-prints. <https://arxiv.org/abs/1805.03221>
- Vrba, F. J., Chugainov, P. F., Weaver, W. B., & Stauffer, J. S. 1993, *AJ*, 106, 1608, doi: [10.1086/116751](https://doi.org/10.1086/116751)
- Weaver, A., Andrews, S. M., Birnstiel, T., et al. 2018, ArXiv e-prints. <https://arxiv.org/abs/1805.06457>
- Weidenschilling, S. J. 1977, *MNRAS*, 180, 57
- Whipple, F. L. 1972, in *From Plasma to Planet*, ed. A. Elvius, 211
- Wilking, B. A., Gagné, M., & Allen, L. E. 2008, Star Formation in the ρ Ophiuchi Molecular Cloud, ed. B. Reipurth, 351
- Wilking, B. A., Meyer, M. R., Robinson, J. G., & Greene, T. P. 2005, *AJ*, 130, 1733, doi: [10.1086/432758](https://doi.org/10.1086/432758)

- Wright, E. L., Eisenhardt, P. R. M., Mainzer, A. K., et al. 2010, AJ, 140, 1868, doi: [10.1088/0004-6256/140/6/1868](https://doi.org/10.1088/0004-6256/140/6/1868)
- Youdin, A. N., & Goodman, J. 2005, ApJ, 620, 459, doi: [10.1086/426895](https://doi.org/10.1086/426895)
- Youdin, A. N., & Shu, F. H. 2002, ApJ, 580, 494, doi: [10.1086/343109](https://doi.org/10.1086/343109)
- Zhang, K., Bergin, E. A., Blake, G. A., et al. 2016, ApJL, 818, L16, doi: [10.3847/2041-8205/818/1/L16](https://doi.org/10.3847/2041-8205/818/1/L16)
- Zhang, K., Isella, A., Carpenter, J. M., & Blake, G. A. 2014, ApJ, 791, 42, doi: [10.1088/0004-637X/791/1/42](https://doi.org/10.1088/0004-637X/791/1/42)
- Zhang, S., Zhu, Z., Andrews, S. M., et al. 2018, ApJL, Zhu, Z., Nelson, R. P., Dong, R., Espaillat, C., & Hartmann, L. 2012, ApJ, 755, 6, doi: [10.1088/0004-637X/755/1/6](https://doi.org/10.1088/0004-637X/755/1/6)

Table 6. DSHARP Observing Log (ALMA Program 2016.1.00484.L)

Name (1)	UTC Date (2)	Config. (3)	Baselines (4)	N_{ant} (5)	$\mathcal{E}/^{\circ}$ (6)	PWV/mm (7)	Calibrators (8)
HT Lup	2017/05/14-04:11	C40-5	15 m – 1.1 km	43	76–77	1.00–1.15	J1517-2422, J1427-4206, J1610-3958, J1540-3906
	2017/05/17-02:12	C40-5	15 m – 1.1 km	49	58–67	0.90–1.05	J1517-2422, J1517-2422, J1610-3958, J1540-3906
	2017/09/24-17:39	C40-8/9	41 m – 12.1 km	39	59–70	0.60–1.15	J1517-2422, J1517-2422, J1534-3526, J1536-3151
	2017/09/24-19:12	C40-8/9	41 m – 12.1 km	39	75–78	0.65–1.05	J1517-2422, J1427-4206, J1534-3526, J1536-3151
GW Lup	2017/05/14-04:11	C40-5	15 m – 1.1 km	43	69–72	1.00–1.15	J1517-2422, J1427-4206, J1610-3958, J1540-3906
	2017/05/17-02:12	C40-5	15 m – 1.1 km	49	51–61	0.90–1.05	J1517-2422, J1517-2422, J1610-3958, J1540-3906
	2017/09/24-23:31	C40-8/9	41 m – 14.9 km	40	29–39	0.80–1.20	J1617-5848, J1733-1304, J1534-3526, J1536-3151
	2017/11/04-14:59	C43-9	113 m – 13.9 km	43	58–69	0.60–0.80	J1427-4206, J1427-4206, J1534-3526, J1536-3151
IM Lup	2017/09/25-20:18	C40-8/9	41 m – 14.9 km	42	67–74	0.85–1.05	J1517-2422, J1517-2422, J1610-3958, J1604-4228
	2017/10/24-18:09	C43-9	41 m – 13.9 km	46	69–75	0.68–0.78	J1517-2422, J1427-4206, J1610-3958, J1604-4228
RU Lup	2017/05/14-04:11	C40-5	15 m – 1.1 km	43	76–78	1.00–1.15	J1517-2422, J1427-4206, J1610-3958, J1540-3906
	2017/05/17-02:12	C40-5	15 m – 1.1 km	49	58–68	0.90–1.05	J1517-2422, J1517-2422, J1610-3958, J1540-3906
	2017/09/29-20:46	C40-8/9	41 m – 15.0 km	43	60–70	1.25–1.65	J1517-2422, J1517-2422, J1610-3958, J1604-4228
	2017/11/21-13:33	C43-8	92 m – 8.5 km	43	52–62	0.35–0.60	J1427-4206, J1427-4206, J1610-3958, J1604-4228
Sz 114	2017/05/14-04:11	C40-5	15 m – 1.1 km	43	72–73	1.00–1.15	J1517-2422, J1427-4206, J1610-3958, J1540-3906
	2017/05/17-02:12	C40-5	15 m – 1.1 km	49	59–67	0.90–1.05	J1517-2422, J1517-2422, J1610-3958, J1540-3906
	2017/09/25-23:57	C40-8/9	41 m – 14.9 km	42	29–39	0.80–1.10	J1924-2914, J1733-1304, J1610-3958, J1604-4228
Sz 129	2017/05/14-04:11	C40-5	15 m – 1.1 km	43	71–74	1.00–1.15	J1517-2422, J1427-4206, J1610-3958, J1540-3906
	2017/05/17-02:12	C40-5	15 m – 1.1 km	49	53–61	0.90–1.05	J1517-2422, J1517-2422, J1610-3958, J1540-3906
	2017/09/24-20:58	C40-8/9	41 m – 14.9 km	40	60–68	0.85–1.15	J1427-4206, J1427-4206, J1610-3958, J1604-4228
	2017/11/22-11:48	C43-8	92 m – 8.3 km	48	32–43	0.35–0.42	J1427-4206, J1427-4206, J1610-3958, J1604-4228
MY Lup	2017/05/14-04:11	C40-5	15 m – 1.1 km	43	69–71	1.00–1.15	J1517-2422, J1427-4206, J1610-3958, J1540-3906
	2017/05/17-02:12	C40-5	15 m – 1.1 km	49	54–61	0.90–1.05	J1517-2422, J1517-2422, J1610-3958, J1540-3906
	2017/09/24-22:14	C40-8/9	41 m – 14.9 km	40	46–57	0.90–1.25	J1427-4206, J1617-5848, J1610-3958, J1604-4228
	2017/11/25-14:35	C43-8	92 m – 8.5 km	44	63–68	0.60–0.80	J1617-5848, J1617-5848, J1610-3958, J1604-4228
HD 142666	2017/09/25-21:31	C40-8/9	41 m – 14.9 km	42	56–69	0.80–1.00	J1517-2422, J1517-2422, J1553-2422, J1609-2205
	2017/11/09-14:47	C43-8	139 m – 13.9 km	44	59–72	0.55–0.80	J1427-4206, J1427-4206, J1553-2422, J1609-2205
HD 143006	2017/05/14-06:00	C40-5	15 m – 1.1 km	43	66–79	0.90–1.05	J1517-2422, J1517-2422, J1625-2527, J1615-2430
	2017/05/17-03:52	C40-5	15 m – 1.1 km	45	73–80	0.80–0.95	J1517-2422, J1733-1304, J1625-2527, J1615-2430
	2017/05/19-02:09	C40-5	17 m – 1.1 km	40	50–66	0.55–0.80	J1517-2422, J1517-2422, J1625-2527, J1609-2205
	2017/09/26-22:36	C40-8/9	41 m – 14.9 km	41	39–52	1.50–1.90	J1517-2422, J1733-1304, J1553-2422, J1609-2205
	2017/11/26-13:59	C43-8	92 m – 8.5 km	45	62–72	0.75–0.85	J1427-4206, J1427-4206, J1553-2422, J1609-2205
AS 205	2017/05/14-06:00	C40-5	15 m – 1.1 km	43	66–80	0.90–1.05	J1517-2422, J1517-2422, J1625-2527, J1615-2430
	2017/05/17-03:52	C40-5	15 m – 1.1 km	45	73–80	0.80–0.95	J1517-2422, J1733-1304, J1625-2527, J1615-2430
	2017/05/19-02:09	C40-5	17 m – 1.1 km	40	50–66	0.55–0.80	J1517-2422, J1517-2422, J1625-2527, J1609-2205
	2017/09/29-22:16	C40-8/9	41 m – 15.0 km	43	44–56	1.20–1.50	J1517-2422, J1733-1304, J1551-1755, J1532-1319
SR 4	2017/05/14-06:00	C40-5	15 m – 1.1 km	43	66–79	0.90–1.05	J1517-2422, J1517-2422, J1625-2527, J1615-2430
	2017/05/17-03:52	C40-5	15 m – 1.1 km	45	73–80	0.80–0.95	J1517-2422, J1733-1304, J1625-2527, J1615-2430
	2017/05/19-02:09	C40-5	17 m – 1.1 km	40	50–66	0.55–0.80	J1517-2422, J1517-2422, J1625-2527, J1609-2205
	2017/09/06-23:08	C40-8	41 m – 7.6 km	47	57–70	0.75–0.90	J1517-2422, J1517-2422, J1625-2527, J1633-2557
	2017/10/17-22:42	C43-10	41 m – 16.2 km	47	27–39	1.40–1.85	J1617-5848, J1733-1304, J1625-2527, J1633-2557
Elias 20	2017/05/14-06:00	C40-5	15 m – 1.1 km	43	66–79	0.90–1.05	J1517-2422, J1517-2422, J1625-2527, J1615-2430
	2017/05/17-03:52	C40-5	15 m – 1.1 km	45	73–80	0.80–0.95	J1517-2422, J1733-1304, J1625-2527, J1615-2430
	2017/05/19-02:09	C40-5	17 m – 1.1 km	40	50–66	0.55–0.80	J1517-2422, J1517-2422, J1625-2527, J1609-2205
	2017/09/23-22:35	C40-8/9	41 m – 12.1 km	39	50–63	0.75–0.90	J1517-2422, J1517-2422, J1625-2527, J1633-2557
DoAr 25	2017/05/10/07-23:10	C43-10	41 m – 16.2 km	51	29–42	0.40–0.80	J1617-5848, J1733-1304, J1625-2527, J1633-2557
	2017/05/14-06:00	C40-5	15 m – 1.1 km	43	67–80	0.90–1.05	J1517-2422, J1517-2422, J1625-2527, J1615-2430
	2017/05/17-03:52	C40-5	15 m – 1.1 km	45	73–80	0.80–0.95	J1517-2422, J1733-1304, J1625-2527, J1615-2430
	2017/05/19-02:09	C40-5	17 m – 1.1 km	40	50–66	0.55–0.80	J1517-2422, J1517-2422, J1625-2527, J1609-2205
Elias 24	2017/09/22-23:11	C40-8/9	41 m – 12.1 km	40	42–54	0.65–1.10	J1517-2422, J1733-1304, J1625-2527, J1633-2557
	2017/09/25-22:42	C40-8/9	41 m – 14.9 km	42	46–58	0.78–1.05	J1517-2422, J1733-1304, J1625-2527, J1633-2557

Table 6 continued

Table 6 (*continued*)

Name (1)	UTC Date (2)	Config. (3)	Baselines (4)	N_{ant} (5)	$\mathcal{E}/^{\circ}$ (6)	PWV/mm (7)	Calibrators (8)
Elias 27	2017/10/04-23:04	C43-10	41 m – 15.0 km	45	34–46	0.85–1.10	J1617-5848, J1733-1304, J1625-2527, J1633-2557
	2017/09/07-22:42	C40-8	41 m – 8.8 km	45	63–76	1.10–1.35	J1517-2422, J1517-2422, J1625-2527, J1633-2557
DoAr 33	2017/10/03-21:56	C43-10	41 m – 15.0 km	45	50–63	0.95–1.15	J1517-2422, J1517-2422, J1625-2527, J1633-2557
	2017/05/14-06:00	C40-5	15 m – 1.1 km	43	66–79	0.90–1.05	J1517-2422, J1517-2422, J1625-2527, J1615-2430
WSB 52	2017/05/17-03:52	C40-5	15 m – 1.1 km	45	73–80	0.80–0.95	J1517-2422, J1733-1304, J1625-2527, J1615-2430
	2017/05/19-02:09	C40-5	17 m – 1.1 km	40	50–66	0.55–0.80	J1517-2422, J1517-2422, J1625-2527, J1609-2205
	2017/09/17-23:06	C40-8/9	41 m – 12.1 km	46	47–59	0.80–1.20	J1517-2422, J1733-1304, J1625-2527, J1633-2557
	2017/10/10-22:26	C43-10	41 m – 16.2 km	47	36–48	0.55–0.75	J1517-2422, J1733-1304, J1625-2527, J1609-2205
	2017/05/14-06:00	C40-5	15 m – 1.1 km	43	66–79	0.90–1.05	J1517-2422, J1517-2422, J1625-2527, J1615-2430
WaOph 6	2017/05/17-03:52	C40-5	15 m – 1.1 km	45	73–80	0.80–0.95	J1517-2422, J1733-1304, J1625-2527, J1615-2430
	2017/05/19-02:09	C40-5	17 m – 1.1 km	40	50–66	0.55–0.80	J1517-2422, J1517-2422, J1625-2527, J1609-2205
	2017/09/10-23:56	C40-8	41 m – 7.6 km	43	43–55	0.50–1.00	J1517-2422, J1733-1304, J1625-2527, J1633-2557
	2017/10/06-22:51	C43-10	41 m – 16.2 km	49	35–47	0.60–0.80	J1616-5848, J1733-1304, J1625-2527, J1633-2557
AS 209	2017/05/09-04:28	C40-5	15 m – 1.1 km	45	67–73	1.00–1.15	J1517-2422, J1733-1304, J1634-2058, J1653-1551
	2017/09/09-00:59	C40-8	41 m – 7.6 km	42	32–45	0.80–1.30	J1751+0939, J1733-1304, J1653-1551, J1658-0739
	2017/09/20-00:36	C40-8/9	41 m – 12.1 km	44	27–41	0.70–1.00	J1751+0939, J1733-1304, J1653-1551, J1658-0739
HD 163296	2017/05/09-04:28	C40-5	15 m – 1.1 km	45	67–74	1.00–1.15	J1517-2422, J1733-1304, J1634-2058, J1653-1551
	2017/09/07-00:24	C40-8	41 m – 7.6 km	46	42–54	0.60–0.85	J1517-2422, J1733-1304, J1653-1551, J1658-0739
	2017/09/20-23:18	C40-8/9	41 m – 12.1 km	44	46–58	0.80–1.50	J1517-2422, J1733-1304, J1653-1551, J1658-0739
	2017/09/08-22:17	C40-8	41 m – 5.8 km	40	79–87	1.10–1.40	J1924-2914, J1924-2914, J1751-1950, J1743-1658
	2017/09/08-23:12	C40-8	41 m – 5.8 km	40	74–87	1.10–1.40	J1924-2914, J1733-1304, J1751-1950, J1743-1658

NOTE—Basic information from the individual execution blocks conducted as part of ALMA Program 2016.1.00484.L. Col. (1) Target name. Col. (2) UTC date and time for the start of the execution block. Col. (3) ALMA configuration. Col. (4) Minimum and maximum baseline lengths. Col. (5) Number of antennas available. Col. (6) Target elevation range. Col. (7) Range of precipitable water vapor levels. Col. (8) From left to right, the quasars observed for calibrating the bandpass, amplitude scale, phase variations, and checking the phase transfer. Additional archival observations used in our analysis are compiled in Table 3.

Table 7. Archival ALMA Datasets

Name	UTC Date	Config.	Baselines	N_{ant}	Calibrators	Program	Refs.
(1)	(2)	(3)	(4)	(5)	(6)	(7)	(8)
IM Lup	2014/07/06-22:18	C34-4	20 – 650 m	31	J1427-4206, Titan, J1534-3526, J1626-2951	2013.1.00226.S	1
	2014/07/17-01:38	C34-4	20 – 650 m	32	J1427-4206, Titan, J1534-3526, ...	2013.1.00226.S	1
	2015/01/29-09:48	C34-2/1	15 – 349 m	40	J1517-2422, Titan, J1610-3958, ...	2013.1.00694.S	2
	2015/05/13-08:30	C34-3/4	21 – 558 m	36	J1517-2422, Titan, J1610-3958, ...	2013.1.00694.S	2
	2015/06/09-23:42	C34-5	21 – 784 m	37	J1517-2422, Titan, J1610-3958, J1614-3543	2013.1.00798.S	3
HD 142666	2015/07/21-22:27	C34-7/6	15 – 1600 m	44	J1517-2422, Titan, J1627-2426, J1625-2527	2013.1.00498.S	...
HD 143006	2016/06/14-03:35	C40-4	15 – 642 m	37	J1517-2422, J1517-2422, J1625-2527, ...	2015.1.00964.S	...
	2016/07/02-04:17	C40-4	15 – 704 m	42	J1517-2422, J1517-2422, J1625-2527, ...	2015.1.00964.S	...
AS 205	2012/03/27-10:08	...	43 – 402 m	15	J1924-2914, Titan, J1625-2527, ...	2011.0.00531.S	4
	2012/05/04-05:11	...	21 – 402 m	15	3C 279, Titan, J1625-2527, ...	2011.0.00531.S	4
Elias 24	2015/07/21-22:27	C34-7/6	15 – 1600 m	44	J1517-2422, Titan, J1627-2426, J1625-2527	2013.1.00498.S	5
Elias 27	2015/07/21-22:27	C34-7/6	15 – 1600 m	44	J1517-2422, Titan, J1627-2426, J1625-2527	2013.1.00498.S	6
AS 209	2014/07/02-03:54	C34-4	20 – 650 m	34	J1733-1304, Titan, J1733-1304, ...	2013.1.00226.S	?
	2014/07/17-02:48	C34-4	20 – 650 m	32	J1733-1304, Titan, J1733-1304, ...	2013.1.00226.S	?
	2016/09/22-23:15	C40-6	xx – 3144 m	38	J1517-2422, J1733-1304, J1733-1304, ...	2015.1.00486.S	7
	2016/09/26-13:02	C40-6	xx – 3144 m	41	J1517-2422, J1733-1304, J1733-1304, ...	2015.1.00486.S	7
HD 163296	2014/06/04-07:10	C34-4	21 – 558 m	33	J1733-1304, J1733-1304, J1733-1304, ...	2013.1.00366.S	8
	2014/06/14-06:20	C34-4	21 – 558 m	35	J1733-1304, J1733-1304, J1733-1304, ...	2013.1.00366.S	8
	2014/06/16-07:09	C34-4	21 – 558 m	35	J1733-1304, J1733-1304, J1733-1304, ...	2013.1.00366.S	8
	2014/06/17-07:25	C34-4	21 – 558 m	30	J1733-1304, J1733-1304, J1733-1304, ...	2013.1.00366.S	8
	2014/06/29-05:44	C34-4	21 – 558 m	32	J1733-1304, J1733-1304, J1733-1304, ...	2013.1.00366.S	8
	2015/08/05-04:15	C34-7/6	42 – 1574 m	37	J1733-1304, Ceres, J1733-1304, J1812-2836	2013.1.00601.S	9
	2015/08/08-03:31	C34-7/6	42 – 1574 m	43	J1733-1304, Ceres, J1733-1304, J1812-2836	2013.1.00601.S	9
	2015/08/09-00:54	C34-7/6	42 – 1574 m	41	J1733-1304, Titan, J1733-1304, J1812-2836	2013.1.00601.S	9

NOTE—Col. (1) Target name. Col. (2) UTC date and time for the start of the execution block. Col. (3) ALMA configuration. Col. (4) Range of baseline lengths. Col. (5) Number of antennas available. Col. (6) From left to right, the quasars observed for calibrating the bandpass, amplitude scale, phase variations, and checking the phase transfer. Col. (7) ALMA program ID number. Col. (8) Published references: 1 = [Huang et al. \(2017\)](#), 2 = [Cleeves et al. \(2016\)](#), 3 = [Pinte et al. \(2018\)](#), 4 = [Salyk et al. \(2014\)](#), 5 = [Dipierro et al. \(2018\)](#), 6 = [Pérez et al. \(2016\)](#), 7 = [Fedele et al. \(2018\)](#), 8 = [Flaherty et al. \(2017\)](#), 9 = [Isella et al. \(2016\)](#).